This is a preprint, the final version is subject to change, of the American Mineralogist (MSA)
Cite as Authors (Year) Title. American Mineralogist, in press.
(DOI will not work until issue is live.) DOI: http://dx.doi.org/10.2138/am-2017-5668

Revision #2

Effects of fluorine content on the elastic behavior of topaz $[Al_2SiO_4(F,OH)_2]$

Gianfranco Ulian and Giovanni Valdrè*

Centro di Ricerca Interdisciplinare di Biomineralogia, Cristallografia e Biomateriali

Dipartimento di Scienze Biologiche, Geologiche e Ambientali, Università di Bologna

Piazza di Porta San Donato 1, 40126 Bologna, Italy

E-mail: giovanni.valdre@unibo.it

Phone: +39-051-2094943 Fax: +39-051-2094943

Abstract

In this work, we modelled the structure, the compressional behavior and the physical properties of topaz over six different fluorine contents and a wide range of pressure, using a quantum mechanical approach based on periodic boundary conditions. We adopted the density functional theory using the B3LYP functional and all-electron Gaussian-type orbitals basis sets. An atomic level description of the athermal (T = 0 K) pressure-induced structural modification of topaz is provided. From the compression results we obtained the athermal bulk modulus (K_{T0}), its first derivative (K') and the athermal volume at zero pressure (V_0) by a third-order Birch-Murnaghan equation fit. The results show that K_{T0} increases with fluorine content. The compressional pattern is anisotropic, as observed by the axial compressibility and second-order elastic constants calculations. We observed that the compression involves three different mechanism, polyhedral contraction, polyhedral tilting and hydrogen bonding, all of them influenced, with different extent, by the fluorine content in topaz. Recent experimental results obtained by single-crystal X-ray and neutron diffraction of specific topaz compositions are in very good agreement with our simulations, which further extend the knowledge of the structural and elastic properties of topaz over a wider range of fluorine content.

Keywords: Topaz, DFT, B3LYP, Equation of state, elastic constants, athermal limit

Introduction

Topaz is an orthosilicate mineral with ideal formula $Al_2SiO_4(F,OH)_2$, which is usually found as an accessory mineral in fluoride-rich granitic rocks related to pneumatolithic/hydrothermal events and in rocks formed in ultrahigh pressure conditions, or in detrital sediments related to areas of acid intrusive rocks (Pichavant and Manning, 1984; Taylor and Fallick, 1997; Alberico et al., 2003). The crystal structure of topaz was firstly solved by Alston and West (1928) and Pauling (1928); more recent studies were focused on solid solution crystal-chemistry of the $Al_2SiO_4F_2$–$Al_2SiO_4(OH)_2$ series (Wunder et al., 1999; Alberico et al., 2003; Chen et al., 2005; Gatta et al., 2006b). In these studies it was shown that natural topaz samples with F:(F,OH) ratio > 1.5 usually crystallize in space group *Pbnm*, with one independent H-site, but synthetic topaz, $Al_2SiO_4(OH)_2$, displays two non-equivalent H-sites. According to the work of Northrup et al. (1994), synthetic topaz belongs to space group $Pbn2_1$, while more recent results of Chen et al. (2005) and Komatsu et al. (2008) suggested space group *Pbnm*.

Due to its composition, topaz is considered one of the major carriers of fluorine and hydroxyl groups, thus playing an important role in the H_2O and F cycles in geological environments. This is particularly true in subduction zones, and in volcanism related to the overlaying subduction wedge.

Topaz is also very appreciated for its mechanical properties, for example, it is used to create abrasives, grindstones, sharpening stones and scouring powders, because of its pronounced hardness (Gatta et al., 2014). This property is due to the high stability at high pressure and temperature. Furthermore, worth to be remembered that topaz is a gemstone, whose optical properties and hardness are employed to assess its quality.

For both geological and industrial reasons, many experimental studies were carried out by high-pressure investigations to depict the mechanical stability of topaz. The behavior of natural topaz at high pressure up to 6 GPa was described by Komatsu et al. (2003), and by Gatta et al. (2006a), up to 10.6 GPa, both of them using *in situ* single-crystal X-ray diffraction. A more recent high-pressure experiment up to 7.5 GPa on synthetic topaz was performed by Komatsu et al. (2008) by neutron

powder diffraction. Among these works there is a slight disagreement between the elastic properties. The bulk modulus at specific temperature (K_{T0}) obtained with a third-order Birch-Murnaghan equation of state (Birch, 1947), BM3, was 154 GPa in the work of Komatsu et al. (2003), while it was 164 GPa in the one of Gatta et al. (2006a). This difference may resides on both the different crystal chemistry [$Al_2SiO_4(OH)_{0.43}F_{1.57}$ and $Al_2SiO_4(OH)_{0.25}F_{1.75}$, respectively] and the first derivative of the bulk modulus (K'), that was kept fixed to 4 by Komatsu and co-workers (2003). However, both studies evinced no phase transition or change of the compressional behavior within the P-range investigated, even if in the work of Gatta et al. (2006a) the P-derivative of K_{T0} ($K' = 2.9$) suggested a deformational configuration that precedes a phase transition. Very recently, Gatta and co-workers (Gatta et al., 2014) extended their investigation up to 45 GPa, finding BM3 parameters $K_{T0} = 158$ GPa and $K' = 3.3$, in good agreement with previous mechanical data (Gatta et al., 2006a). However, the authors suggested a possible phase transition at higher pressure (*i.e.*, P in excess of GPa) because of the value of $K' < 4$.

Despite the presence of some works on the elastic properties of natural and synthetic topaz, none of them proposed to correlate them with the value of the F:OH ratio in the structure. It is known that the physical, structural and thermodynamic properties of topaz are controlled by the hydroxyl content (Akizuki et al., 1979; Barton, 1982; Barton et al., 1982; Tsareva et al., 1992). In natural samples, it is often difficult to find extensive OH substitutions, which depend on the mineral formation environment (Zhang et al., 2002), but it is possible to obtain synthetic fully hydrated topaz end-members at ca. 7 GPa (Wunder et al., 1993). In order to explore the effects of different F:OH ratios on topaz structural and mechanical properties and to gain a better understanding of the compressional behavior of topaz, we undertook a quantum-mechanical simulations of topaz models with different fluorine content up to very high-pressures (50 GPa). Furthermore, the quantum mechanical approach will investigate the first derivative of bulk modulus that, as mentioned above, is still a subject to be clarified.

Computational Details

This study was conducted by first principle simulations on periodic systems, using the CRYSTAL09 code (Dovesi et al., 2009), which implements the Hartree–Fock and Kohn–Sham self-consistent field method. The graphical drawings have been carried out with the molecular graphics software MOLDRAW (Ugliengo et al., 1993) and VESTA (Momma and Izumi, 2011).

The calculations have been performed within the Density Functional Theory, using the hybrid exchange functional (B3LYP), which is composed by the Becke three-parameters (Becke, 1993) and the Lee, Yang and Parr (Lee et al., 1988) gradient-corrected correlation functionals. The exchange–correlation contribution is calculated over a grid of points and is the result of a numerical integration of the electron density and its gradient. To improve the accuracy/computational costs ratio for geometry optimizations, a 75 points × 974 angular points pruned grid (XLGRID keyword) obtained from the Gauss–Legendre quadrature and Lebedev schemes (Prencipe et al., 2004) was used. The values of the tolerances that control the Coulomb and exchange series are the default provided by CRYSTAL09, but we increased the pseudo-overlap parameter from 12 to 14 (Dovesi et al., 2009) to stabilize the self-consistent behavior during unit-cell deformations. The Hamiltonian matrix has been diagonalized (Monkhorst and Pack, 1976) using a shrinking factor (*IS*) = 4 (Dovesi et al., 2009), that leads to a 4×4×4 k-mesh and 36 k-points.

Within the CRYSTAL code, multi-electron wave functions are described by linear combination of crystalline orbitals (CO), expanded in terms of Gaussian-type orbital (GTO) basis sets. The basis sets have been previously optimized by various authors for their investigations of similar structures. For all the calculations, oxygen has been described by a 8-411d11G basis sets (Ulian et al., 2013b; Ulian et al., 2014b; Valenzano et al., 2006), aluminum atoms by a 8-511d1G basis set (Catti et al., 1994), silicon by a 88-31G* (Nada et al., 1996; Ulian et al., 2014a) and fluorine atoms by a 7-311G

basis set (Nada et al., 1993). Hydrogen was described by a standard 3-1p1G basis set with *p* polarization function exponent of 1.1 $Bohr^{-1}$, which was employed in previous simulations of urea crystals (Gatti et al., 1994) and phyllosilicates (Ulian et al., 2013a; Ulian et al., 2014a; Ulian and Valdrè, 2015b; Ulian and Valdrè, 2015c). The chosen hydrogen atom basis set allows accurate calculations of hydrogen atoms in molecular and crystal structures and it is well balanced with the other atomic basis sets used in topaz structures.

Lattice constants and internal coordinates have been optimized within the same run using the analytical gradient method for the atomic positions and a numerical gradient for the unit-cell parameters. The Hessian matrix is upgraded with the BFGS algorithm (Broyden, 1970a; Broyden, 1970b; Fletcher, 1970; Goldfarb, 1970; Shanno, 1970). The tolerances for the maximum allowed gradient and the maximum atomic displacement for considering the geometry as converged have been set to $6 \cdot 10^{-5}$ hartree $bohr^{-1}$ and $12 \cdot 10^{-5}$ bohr, respectively. These values are stricter than the default ones provided by CRYSTAL09 (Dovesi et al., 2009), because mechanical properties evaluations require the structure in analysis as close as possible to the structure corresponding to the minimum of the potential energy.

Results and discussion

Effect of fluorine on the topaz structure

The rationale of the modelling of F content in topaz can be summarized as follows. We created the basic topaz structural model (lattice parameters, Si, Al and O positions) from recent experimental X-Ray diffraction results by Gatta et al. (2006b). Topaz unit cell presents four unit formulas of $Al_2SiO_4(F,OH)_2$ ($Z = 4$), resulting in eight sites that can be occupied by either hydroxyl groups or by fluorine. This feature would allow to simulate several models that present different F:OH ratios.

We decided to model six different topaz unit cells with different F:OH ratio, reported as follows:

1. F:OH ratio = 0:2 – model labeled as T-F0H8 (symmetry *Pbnm* and $Pbn2_1$, Fig.1a)

2. F:OH ratio = 0.5:1.5 – model labeled as T-F2H6 (symmetry *P1*, Fig.1b)
3. F:OH ratio = 1:1 – model labeled as T-F4H4 (symmetry $Pbn2_1$ and *P1*, Fig.1c)
4. F:OH ratio = 1.5:0.5 – model labeled as T-F6H2 (symmetry *P1*, Fig.1d)
5. F:OH ratio = 1.75:0.25 – model labeled as T-F7H1 (symmetry *P1*, Fig.1e)
6. F:OH ratio = 2:0 – model labeled as T-F8H0 (symmetry *Pbnm*, Fig.1f)

In quantum mechanical solid solution modelling, end-members usually have the highest symmetry, whereas intermediate compositions belong to space groups with the same or lower symmetry. This happens because high-symmetry operators could create unphysical replica of atoms in the unit cells and it is not possible to consider atomic partial occupancies. Other reasons of the space group assigned to each model are explained below.

We optimized the geometry of the topaz models (lattice and atomic coordinates) within the DFT method explained in the computational section. For the sake of clarity, lattice parameters, crystallographic volume (V_{cc}) and density are reported in Table 1, alongside data from diffraction experiments taken from literature.

The first concern was about the full-hydroxyl topaz space group (model T-F0H8) for the controversy in literature of the model. Fully hydroxylated topaz unit cell contains two hydrogen sites, namely H1 and H2, which have to be investigated because they can deeply affect the mineral stability and structure. We considered three possible hydrogen configurations in T-F0H8 model: H1 – H1, H1 – H2 and H2 – H2. The first and the last belongs to *Pbnm* space group (7 irreducible atoms in the unit cell), whereas H1 – H2 configuration can be described by $Pbn2_1$ space group (11 irreducible atoms in the unit cell). Each described model with different hydrogen configuration and has been created and optimized to find out which one is energetically the most stable. The results are reported in Table 2. The three configurations have many differences in lattice parameters due to the hydrogen position. It can be observed that the models with 100% occupancy of H1 and H2 sites are less stable than the one with half H1 sites and half H2 sites. In H1 – H1 configuration there is a quite small H --- H distance (~2Å), which results in hydrogen atom repulsion and, then,

destabilization of the structure. On the opposite, the hydrogen atom distance is higher in H2 – H2 configuration, but there is a shorter H --- Al distance. In addition, the H2 – H2 configuration is not maintained during optimization, as the structure spontaneously evolves toward the H1 – H1 configuration because of the symmetry constrain (the result reported in Table 2 represents a situation similar to a saddle point in the potential energy surface of the hydrogen configurations). According to our results, the full-hydroxyl topaz is more stable with H1 and H2 sites with 50% occupancy each, with H --- H distance of about 2.3 Å. This structure loses the mirror plane operator, lowering its symmetry from *Pbnm* to $Pbn2_1$, in agreement with the results of Northrup et al. (1994). From now on, discussion on model T-F0H8 will be made on the model with H1 – H2 configuration.

For model T-F8H0, fully fluorinated topaz, we employed the space group *Pbnm* (6 irreducible atoms in the unit cell) because it was previously assigned by experimental XRD redacted (Gatta et al., 2006b). For all other structures, we performed an initial analysis of configurations (D'Arco et al., 2013; Mustapha et al., 2013) to find the OH^-/F^- substitution locations that maximizes the internal symmetry. Only the T-F4H4 model, where half sites are occupied by fluorine and half by hydroxyl groups, presents a high-symmetry configuration related to space group $Pbn2_1$. We investigated this crystal configuration, optimizing the structure with both high ($Pbn2_1$) and low (*P1*) symmetry, finding almost no differences between the results obtained with the different space groups for both structure and equation of state (see below). When symmetry constraints are removed, there is a negligible reduction of unit cell axes (max –0.02%) and volume (–0.04%), but angular values are very close to 90° (variations of max $9 \cdot 10^{-5}$ degrees). The energy difference between the two structures is again below experimental uncertainties ($E_{Pbn21} - E_{P1}$ = 1.6 kJ/mol). We decided to employ the $Pbn2_1$ space group for model T-F4H4 in order to keep consistency with the other crystal structures. As done for the T-F0H8 model, the occupancy of both H1 and H2 sites has been considered. However, we found that the H2 site is not stable, with the hydrogen atom moving to the H1 site.

Atomic fractional coordinates for the topaz structures with internal order, T-F0H8 ($Pbn2_1$), T-F4H4 ($Pbn2_1$) and T-F8H0 (*Pbnm*) are presented in Table 3, alongside experimental diffraction data from Northrup et al. (1994). It can be observed a very good agreement in the atomic disposition in the unit cell.

All the remaining models, T-F2H6, T-F6H8 and T-F7H1, were simulated without any internal symmetry (space group *P1*) because of the reduction of the internal order in the model unit cells. It is worth to be remembered that single-crystal XRD refinements usually reports structures with partial atomic occupancies and the hydrogen atom positions are not easily determined. Regarding the occupancy of H1 and H2 sites, we found that in T-F2H6 model the half occupancy is favored, as in T-F0H8 structure, but in the other two models the most stable hydrogen configuration is H1. Our simulations clarify that in F-rich topaz (F:OH ratio ≥ 50%) only H1 site is occupied, as H2 is not stable.

Starting from the fully-hydroxilic topaz model, it can be observed that increasing the fluorine content affects the topaz internal structure. In Fig. 2 we reported the topaz unit cell volume (a), relative axial variations (b) and mineral density (c) as a function of F content per unit formula. The unit cell volume monotonically reduces as fluorine atoms substitute hydroxyl groups (Fig. 2a) and the density monotonically increases (Fig. 2c), but it can be observed that the unit cell contraction is not linear. Considering the axis lengths relatively to the full hydroxyl model (see Fig. 2b), the simulations showed a subtle interplay that regulates the final cell volume. The *a* parameter always shrinks as the F:OH ratio is shifted to fluorine (max -1.6%). The **b**- and **c**-axis have a low decrease until F:OH ratio 1:1, then the *b* parameter linearly decreases of about 1% the starting value and the *c* lattice parameter increases of about +0.4%. Overall, the initial contraction of the *a* lattice parameter almost compensates the **b**- and **c**-axis variations, which explains the almost monotonic contraction of the topaz unit cell. Compared to the previous analysis of Alberico et al. (2003), we find a good agreement with their correlation of fluorine content versus lattice parameters. In the cited work, 33 reported data were fitted by least-square procedure to obtain regression lines of cell

edges variations as a function of F content. The authors found a linear relationship regarding both *a* and *b* cell parameters, but the **c**-axis lacks this correlation because this cell edge seems to be constant with increasing fluorine content. This observation was explained by the F(O) --- F(O) contact, which influences mostly the *c* lattice parameter. Our results provide further details in the region that was not covered by the work of Alberico et al. (2003) because of the lack of experimental data regarding topaz structures with fluorine content between 0.0 and 0.5. Regarding the internal geometry, fluorine atoms reduce both the distortion index of $Al(O,F)_6$ groups (see the definition of distortion index by Baur (1974)) and the octahedron volume because of the shrinking of the Al – (O,F) bonds.

In T-F0H8 model we found that the hydroxyl group in H1 site (O4 – H1, see Table 3 and Fig. 1) establishes a hydrogen bond with the oxygen O1 of the other OH group (O4 – H1 --- O1) at distance 2.26 Å. The OH group in H2 site establishes two hydrogen bonds with the oxygen atom of the H1 site (2.17 Å) and the oxygen atom of the SiO_4 tetrahedron bridging two $Al_2O_4(OH)_2$ octahedrons (1.88 Å). This result is in good agreement with the theoretical prediction made by Churakov and Wunder (2004), where the authors employed the generalized gradient approximation (GGA) functional BLYP and atomic basis sets with pseudopotentials to investigate the proton position in the end-member $Al_2SiO_4(OH)_2$ topaz. Unfortunately, in that work only atomic coordinates were relaxed, while lattice parameters were fixed to the experimental refinement values, because of the tendency of GGA functionals to overestimate unit-cell volumes. To our knowledge, no other theoretical works on topaz structure are present in literature. In T-F4H4 model (space group $Pbn2_1$), where there is only one non-equivalent hydroxyl group per unit-cell, the O5 – H1 --- O2 distance is greater (2.2 Å) and the hydrogen bonding is weaker than the O4 – H1 --- O1 one in T-F0H8 model (see Fig. 1). In general, topaz structures that have hydroxyl groups in their unit cell presents at least one H-bond for each hydroxyl group.

Our results for models T-F7H1 [$Al_2SiO_4F_{1.75}(OH)_{0.25}$, *P1*] and T-F0H8 [$Al_2SiO_4(OH)_2$, *Pbnm*] are in good agreement with experimental ones, obtained by *in situ* single-crystal diffraction

experiments on $Al_2SiO_4(OH)_{0.25}F_{1.75}$ (Gatta et al., 2006b) and $Al_2SiO_4(OH)(OD)$ (Komatsu et al., 2008), respectively, both belonging to the *Pbnm* space group. Atomic fractional coordinates satisfactorily match those reported by the authors in their works. We observe in our theoretical data a unit cell volume greater (of about 3%) than that observed from diffraction results. This effect is due to the computational approach, where the B3LYP functional generally overestimates unit cell volumes of about this percentage.

Topaz compression

We adopted the methods proposed by Perger (2010) to describe the compressional behavior of topaz within the periodic boundary conditions used in our simulations. The first step of this procedure is considering different unit-cell volumes of the crystal structures, smaller than the equilibrium geometry volume. Then, the second step requires an optimization of the internal coordinates and lattice parameters for each selected volume, keeping that unit-cell volume constant. This procedure is known as "*symmetry preserving, variable cell-shape structure relaxation*" (Kiefer et al., 2001; Ottonello et al., 2009; Ulian et al., 2014a; Ulian and Valdrè, 2015a; Ulian and Valdrè, 2015c). In our simulations the topaz structures were geometrically optimized at several volumes between the equilibrium geometry, V_{eq}, and 80% · V_{eq}, with a step of 1% V_{eq}. Volumes and lattice parameters from this operation are reported in Table 3 for each simulated topaz structure, whereas all the atomic positions can be found in the crystallographic information framework (CIF) data file.

From the geometry optimizations, the total energy E (Ha, Hartree – atomic unit of energy, 1 Ha = $4.35974434 \cdot 10^{-18}$ J) at constant volume V (Å^3) at each volume for the different topaz models was calculated and the energy *vs* volume dependence, *E(V)*, is well described by a 3rd-order polynomial equation. In Figure 3a plots of the $\Delta E = E(V) - E(V_{eq})$ versus volume for the different topaz models are reported. The static pressure (P_{st}) values for each selected volume can be obtained from the first derivative of the *E(V)* function, according to:

$$P_{st} = -\left(\frac{\partial E}{\partial V}\right)_{T=0} \quad (1)$$

A graphical representation of the relative compression, defined as V/V_0 (here V_0 is the equilibrium geometry), as a function of P_{st} for all the different topaz models is shown in Figure 3b. From the plot, it is possible to note that the pressure versus volume trend is monotonic, without any abrupt changes that would indicate variations in the mineral internal stability. These pressure values are labelled as P_{st} in each table because atomic vibrational energy was not taken into account. This is also called "athermal" condition, because it is like studying "frozen" atoms at absolute zero (0 K). Again, there is a very good agreement between the simulated compression of models T-F7H1 [$Al_2SiO_4F_{1.75}(OH)_{0.25}$] and T-F0H8 [$Al_2SiO_4(OH)_2$] in the 0 – 10 GPa range with the results of Gatta et al. (2006b) and Komatsu and co-workers (2003) referring to the same mineral composition, respectively (see Figure 3c). In the pressure range considered, the two models have very similar compressional behavior, whereas the fully hydrated topaz (T-F0H8) and model T-F6H2 exhibit a slightly softer nature. However, at higher pressure (15 – 50 GPa, see Figure 3d) T-F0H8 seems to increase its stiffness compared to the more fluorinated structures. Above 45 GPa, the models with F content > 6 atoms show very similar mechanical behavior.

In order to obtain the topaz bulk moduli at 0 K (K_0), its pressure first derivative (K') and the volume at zero pressure (V_0), we fitted the volume *vs*. P_{st} data for each structure using a third-order finite strain isothermal Birch-Murnaghan Equation of State (III-BM EOS) (Birch, 1947). The III-BM EOS is defined as:

$$P_{III-BM} = \frac{3}{2} K_{T0} \left[\eta^{-7/3} - \eta^{-5/3}\right] \left\{1 - \frac{3}{4}\left(4 - K'\right)\left(\eta^{-2/3} - 1\right)\right\} + P_0 \quad (2)$$

where $\eta = V/V_0$ and P_0 is the reference pressure (P_0 = 0.0 GPa). The fitting was made by a least-square procedure using the EOS-FIT5.2 software (Angel, 2001). The refined elastic parameters are reported in Table 4. We also investigated T-F4H4 model in absence of internal symmetry (*P1*), founding K_0 = 161 ± 3 GPa, K' = 3.4 ± 0.4 and V_0 = 357.7 ± 0.8 Å^3, whereas employing space

group $Pbn2_1$ the III-BM results are K_0 = 165 ± 3 GPa, K' = 3.4 ± 0.4 and V_0 = 357.6 ± 0.9 Å^3. This small difference between the results calculated with and without internal symmetry arises from the obtained relaxation energy of the model unit cell, which is reflected on the pressure for each volume calculated. The low-symmetry T-F4H4 model is slightly more stable that the high-symmetry one because of the absence of any constraint to the relaxation process, and this explains the lower bulk modulus found for the *P1* structure. However, we observed that there are negligible variations on the atomic positions in the unit cell, even at very high pressures, and this allows considering the two results comparable.

Fig.4 shows the monotonic evolution of the relative compression of topaz lattice parameters with pressure. The graph indicates that the deformation is slightly anisotropic for each model at ca. 50 GPa, with *a* and *c* cell parameters shrank of about 8% the initial size, while the *b* one is reduced by about 6% at the same pressure. Very interesting features may be evinced by making a comparison between the different models. On one hand, fluorine content negligibly influence both *b*- and *c*-axis compressional behaviors, as the lattice parameters almost reach the same relative compressional value of 0.96 and 0.92 at ca. 50 GPa, respectively. On the other hand, lattice parameter *a* behaves similarly to the *c* one in T-F0H8, T-F7H1 and T-F8H0 models, but it seems stiffer in the other structures. In order to describe the observed anisotropy, we calculated the axial bulk moduli with a linear III-BM EOS fit of the lattice parameters values at different pressures. The obtained refined data for the *a*, *b* and *c* axis are reported in Table 4. The axial compressibilities, described as $\beta = 1/3K_0$, are in ratio β(a): β(b): β(c) 1.218 : 2.010 for T-F0H8; 1.345 : 2.071 for T-F2H6; 1.651 : 2.008 for T-F4H4; 1.651 : 1.776 for T-F6H2; 1.590 : 1.624 for T-F7H1 and 1.576 : 1.513 for T-F8H0. It is worth noting that increasing the fluorine content in topaz results in an increase of the β(a) / β(c) ratio (from 0.60 in T-F0H8 model to 1.04 in T-F8H0 one), which means that **a-** and **c-**axis compressibilities become similar by increasing the F content.

The atomic-scale compression mechanism can be better understood from the internal geometry variations at different pressures. When no pressure is imposed on the topaz model, we observed a

monotonic reduction of the unit cell volume by augmenting the fluorine content, because F atoms reduce the Al-octahedron volumes due to its higher electronegativity than oxygen atoms. Our simulations show that the unit-cell volume reduction is anisotropic, with the **a-**axis shrinking almost monotonically, *b* lattice parameter remains almost constant until half sites occupied by F then it reduces and **c-**axis showing opposite length variations than the **b-**axis (see Fig.2b).

For what concerns topaz behavior under pressure, as also reported by Gatta et al. (2006a), the mineral responds to mechanical compression by polyhedral contraction and tilting. We reported specific bond lengths, bond angles and polyhedral volumes in Table 5 that have been analyzed in details. Increasing pressure causes the reduction of Al-O and Si-O bond lengths, with shrinking of about 6% and 4% above 50 GPa, respectively. The first effect related to the mechanical compression is, consequently, Al octahedrons and Si tetrahedrons volumes contraction by 15% and 11%, respectively, at the highest pressure explored. We noted that the distortion index of the $Al(O,F)_6$ octahedron was reduced by about 50% from 0 to 50 GPa, while the index of SiO_4 tetrahedron raised by about 30%. In agreement with the work of Gatta et al. (2006a), it is possible to observe along the [100] direction an alternation of tetrahedra and octahedra in the topaz structure, with highly compressible "weak zones" where there are no Si tetrahedra. Then, topaz compression along the **c-**axis (i.e., perpendicularly to the "weak zones") results more favored than along the other directions. However, the $Al(O,F)_6$ polyhedral contraction is reduced by increasing the fluorine content, and this gives rise to the second compression mechanism, namely the polyhedral tilting. This effect is very pronounced, as can be observed by the Al-(O,F)-Al angles. The $Al(O,F)_6$ tilt at the maximum pressure investigated is about 5%, 8% and 10% in T-F0H8, T-F4H4 and T-F8H0, respectively.

Our simulations suggest that both compression responses, polyhedral contraction and tilting, are affected by the fluorine content. The fluorine ions that substitute OH groups induce a reduction of the $Al(O,F)_6$ internal bond lengths, thus polyhedral volumes shrank.

A third effect is related to the hydrogen bonding scheme in the topaz structure. In all topaz models that contain OH in the unit cell, we observed a negligible variation of the O – H bond length (-0.8% and -0.6%, respectively) at ca. 50 GPa. Mean H-O-Al angle was almost constant with pressure in $Al_2SiO_4(OH)_2$ (T-F0H8) structure, while in $Al_2SiO_4F(OH)$ (T-F4H4) it increased by about 5%. This angular variation probably arises because of the high electronegativity of fluorine, which attracts the hydrogen atom of the OH group. It is also worth remembering that in the low-F content topaz models each hydroxyl group establishes two hydrogen bond with SiO_4 tetrahedra (with H-bond cutoff distance at 2.2 Å). We observed that by increasing pressure, in each topaz model that contains OH group, a bifurcated H bond is established for H1 sites, one with an oxygen atom from SiO_4 tetrahedron and one with another oxygen atom or with a fluorine atom of the Al-octahedron, and a trifurcated bond is established for the H2 sites, two with silica tetrahedra and one with Al-octahedron. Our observations about the formation of hydrogen bonds are in good agreement with the results reported by Komatsu et al. (2008) for the $Al_2SiO_4(OD)_2$ end member topaz, albeit the authors considered a bonding scheme based on the O---O distances.

In this work we firstly investigated the different effects of fluorine content on the physical-chemical properties of topaz and our results give a general vision of the system. In this sense our data extend those reported by Gatta et al. (2014) and by Komatsu et al. (2003, 2008) that refer only to topaz samples of composition $Al_2SiO_4F_{1.75}(OH)_{0.25}$, $Al_2SiO_4F_{1.57}(OH)_{0.43}$ and $Al_2SiO_4(OD)_2$ respectively. For the sake of brevity and conciseness, we limited this study to the athermal limit properties of topaz. The vibrational properties and thermodynamic data of topaz phases would be subject of a subsequent paper (part 2) to extend the knowledge of this complex solid-solution mineral.

Topaz elastic constant tensor

We also calculated the elastic constants of the considered topaz models because they are important mechanical quantities that can be used for geomechanical and technological applications of topaz.

These quantities are rarely reported in literature for minerals and simulated data can help filling this gap and could be useful to the interested reader.

The second-order elastic constants (SOEC) are calculated using stress-strain relationships based on total energy calculations through a Taylor expansion in terms of the strain components truncated at the second order:

$$E(V,\varepsilon) = E(V_0) + V\sum_{\alpha}\sigma_{\alpha}\varepsilon_{\alpha} + \frac{V}{2}\sum_{\alpha\beta}C_{\alpha\beta}\varepsilon_{\alpha}\varepsilon_{\beta} + \ldots, \quad (3)$$

where σ is the stress, ε is the strain, C are the second order elastic constants and V_0 is the volume at equilibrium. Note that we used the Voigt's notation (Nye, 1957), where $\alpha,\beta = 1,2,3,\ldots 6$. The adiabatic SOEC are related to the strain second derivatives of the total energy E according to:

$$C_{\alpha\beta} = \frac{1}{V}\frac{\partial^2 E}{\partial\varepsilon_{\alpha}\partial\varepsilon_{\beta}}\bigg|_0 \quad (4)$$

Their discrete values may be calculated by imposing a certain amount of strain ε along the crystallographic direction corresponding to the component of the dynamical matrix. The evaluation of elastic constants for an arbitrary crystal then requires to accurately calculate derivatives of the total energy as a function of crystal deformation. To facilitate the calculation of the different energy *vs* strain curves and the SOEC, a fully automated numerical procedure was implemented in the CRYSTAL code, under the keyword ELASTCON. Briefly, the proposed algorithm uses the optimized structure and its space group to determine the necessary deformations in order to calculate the various elastic constants. For further details on the ELASTCON method we suggest the reader to refer to the work of Perger et al. (2009). The algorithm was used with good results in the calculation of the thermo-chemical and thermo-physical properties of $BaTiO_3$, rutile TiO_2 and talc (Narejo and Perger, 2010; Narejo and Perger, 2011; Ottonello et al., 2010; Ulian et al., 2014a). In the present work, we chose to run the calculation with three points of displacement and a step of 0.010 Å, the default figure given by the code.

We report in Table 6 the second order elastic constant tensor *C* of the different topaz models, calculated at zero pressure and in athermal conditions (values are in GPa). From literature, the only available elastic constants data regards the full fluorinated topaz ($Al_2SiO_4F_2$), reported in the experimental work of Haussuhl (1993). The simulated results of T-F8H0 model ($Al_2SiO_4F_2$) are in very good agreement with the experimental ones (also reported in Table 6), with only small deviations. Unfortunately, to the authors' knowledge, no other experimental or theoretical results are currently available for the other solid solutions.

The bulk (K) and shear (μ) moduli are related to the elements of the elastic constant tensor. For any crystal system, the bounds for bulk modulus (upper =K_V; lower = K_R) and shear modulus (upper = μ_V; lower = μ_R) are given by the Voigt and Reuss equations (Nye, 1957):

$$K_V = (1/9)\left[C_{11} + C_{22} + C_{33} + 2\left(C_{12} + C_{13} + C_{23}\right)\right] \quad (5)$$

$$K_R = \left[S_{11} + S_{22} + S_{33} + 2\left(S_{12} + S_{13} + S_{23}\right)\right]^{-1} \quad (6)$$

$$\mu_V = (1/15)\left[C_{11} + C_{22} + C_{33} + 3\left(C_{44} + C_{55} + C_{66}\right) - \left(C_{12} + C_{13} + C_{23}\right)\right] \quad (7)$$

$$\mu_R = \frac{15}{4\left[S_{11} + S_{22} + S_{33} - \left(S_{12} + S_{13} + S_{23}\right)\right] + 3\left(S_{44} + S_{55} + S_{66}\right)} \quad (8)$$

where $\left[S\right] = \left[C\right]^{-1}$, the compliance tensor, is the inverse of SOEC tensor *C*.

In topaz there is a small difference between the upper and lower bounds for both bulk and shear moduli, ca. 4 GPa and 2 GPa, respectively, because of the observed anisotropy. It is known that both bulk and shear moduli fall between the two bounds, according to the Voigt-Reuss-Hill averaging method (Hill, 1952):

$$\bar{K}_{VRH} = (1/2)\left(K_V + K_R\right) \quad (9)$$

$$\bar{\mu}_{VRH} = (1/2)\left(\mu_V + \mu_R\right) \quad (10)$$

where $\bar{K}_{VRH}$ and $\bar{\mu}_{VRH}$ are the Voigt-Reuss-Hill averages of the bulk and shear moduli, respectively.

In general, there is a quite good accordance between K_{T0} data calculated from BM3 equation of state and K_R from elastic constants. It can be observed a systematic shift between the two results with absolute variations in the 3 – 7 % range. This means that there is an adequate self-consistency of the proposed simulation methods. All the other values for all the models are reported in Table 6. With these data, it is possible to estimate the Young's modulus, E, using the following expression:

$$E = \frac{9\bar{K}_{VRH}\bar{\mu}_{VRH}}{3\bar{K}_{VRH} + \bar{\mu}_{VRH}} \quad (11)$$

The isotropic Voigt-Reuss-Hill average gives the mean shear and longitudinal wave velocities for hypothetical topaz aggregates with random crystallographic preferred orientation, as

$$\bar{v}_s = \sqrt{\bar{\mu}_{VRH}/\rho} \quad (12)$$

$$\bar{v}_p = \sqrt{\frac{4\bar{K}_{VRH} + 3\bar{\mu}_{VRH}}{3\rho}} \quad (13)$$

where ρ is the density of the crystal. The v_p/v_s ratio is 1.7 for the six considered models.

Implications

The knowledge of the structural and mechanical properties of topaz are important for several reasons that may attract the interest of many scientists in various and different research fields.

First of all, topaz is a mineral characterized by F/OH substitutions and here we present data that shows the correlation between the hydroxyl/fluoride content and the structure-properties relationships. This kind of analysis is important for several Earth materials that present hydroxyl groups, such as hydroxylapatite, and where the substitution of these groups show a dramatic change in their properties. We provided a detailed description of both atomic structure and bonding environment, which could potentially lead to a better understanding of the underlying crystal chemistry that leads to the property changes.

Secondly, topaz occurs as accessory mineral in F-rich granitic rocks at the latest stage of the magma crystallization, often related to the formation of pneumatolithic/hydrothermal deposits, or in rock

formations that experience ultra-high-pressure metamorphism. Natural topaz samples usually contains about 30% of the F sites occupied by hydroxyls, and only in some very rare cases OH-dominant members have been described. Almost nothing is known for other F:OH ratios in topaz solid solution, and in this paper we tried to fill this gap. Even though topaz is an accessory mineral, it is one of the major carriers of F/OH in rocks with granitic origin and thus warrants a detailed study of its high-pressure and high-temperature behavior, if we want to understand the water and fluorine cycles in geological environments, such as subduction zones, and the volcanism in the overlying subduction wedge. The chemical, structural and mechanical properties, alongside thermodynamic ones, are of utmost importance for the interpretation of both phase equilibria and the pressure-temperature rock forming conditions, in particular in the subduction zones. The elastic parameters (i.e., the bulk modulus and the compressional scheme) obtained in this study are in good agreement with previous data reported in literature. Despite the exploration of the compressional behavior of topaz above 50 GPa, the bulk modulus P-derivative is confirmed to be lower than 4. No evidence of phase transition or change in the compressional behavior of topaz was observed within the P-range investigated here.

Thirdly, topaz is an appreciated gemstone for its hardness, durability and optical properties and gemologist may find very useful detailed cross-correlated data on chemical, structural and mechanical properties of this gemstone. It is known that some imperial topaz gemstones can be difficultly distinguished from citrine, a yellowish variety of quartz and, furthermore, white topaz is commonly used as diamond simulant. Furthermore, topaz exhibits a very pronounced hardness (H8, Mohs' scale), which allows considering it as a "ceramic material" and leads to a series of industrial applications (for example, manufacture of grindstones, sharpening stones and scouring powders). For all these reasons, geological, gemological and industrial applications of this mineral would benefit from an extensive study of its cross-correlated intrinsic properties.

Finally, the last but not the least, this quantum mechanical approach to solve solid solution in minerals is one of the first and few that has been employed. This paper demonstrates that chemical,

structural, mechanical and in future thermodynamic data can be obtained for solid solutions in minerals. These results are extremely useful and attractive for mineralogists and petrologists interested in thermodynamic properties of topaz, information that can not be, in some cases, available from experimental methods because of the lack of specific samples and complex instrumentations.

Acknowledgments

The authors wish to thank the University of Bologna for funding.

References

Akizuki, M., Hampar, M.S., and Zussman, J. (1979) An explanation of anomalous optical properties of topaz. Mineralogical Magazine, 43(3269), 237-241.

Alberico, A., Ferrando, S., Ivaldi, G., and Ferraris, G. (2003) X-ray single-crystal structure refinement of an OH-rich topaz from Sulu UHP terrane (Eastern China) - Structural foundation of the correlation between cell parameters and fluorine content. European Journal of Mineralogy, 15(5), 875-881.

Alston, N.A., and West, J. (1928) The structure of topaz. Proceedings of the Royal Society A, 121, 358-367.

Angel, R.J. (2000) Equations of state. In: Hazen RM, Downs RT, Eds, High-temperature and high-pressure crystal chemistry. Reviews in Mineralogy and Geochemistry, 41, 35-60.

Barton, M.D. (1982) The thermodynamic properties of topaz solid solutions and some petrologic applications. American Mineralogist, 67(9-10), 956-974.

Barton, M.D., Haselton Jr, H.T., Hemingway, B.S., Kleppa, O.J., and Robie, R.A. (1982) The thermodynamic properties of fluor-topaz. American Mineralogist, 67(3-4), 350-355.

Baur, W.H. (1974) The geometry of polyhedral distortions. Predictive relationships for the phosphate group. Acta Crystallographica, Section B: Structural Science, 30, 1195-1215.

Becke, A.D. (1993) Density-Functional Thermochemistry .3. The Role of Exact Exchange. Journal of Chemical Physics, 98(7), 5648-5652.

Birch, F. (1947) Finite elastic strain of cubic crystal. Physical Review, 71, 809-824.

Broyden, C.G. (1970a) The convergence of a class of double-rank minimization algorithms 1. General considerations. IMA Journal of Applied Mathematics, 6(1), 76-90.

-. (1970b) The convergence of a class of double-rank minimization algorithms: 2. The new algorithm. IMA Journal of Applied Mathematics, 6(3), 222-231.

Catti, M., Valerio, G., Dovesi, R., and Causa, M. (1994) Quantum-mechanical calculation of the solid-state equilibrium MgO + alpha-Al_2O_3 $MgAl_2O_4$ (spinel) versus pressure. Physical Review B, 49(20), 14179-14187.

Chen, J.R., Lager, G.A., Kunz, M., Hansen, T.C., and Ulmer, P. (2005) A Rietveld refinement using neutron powder diffraction data of a fully deuterated topaz, Al2SiO4(OD)(2). Acta Crystallographica Section E-Structure Reports Online, 61, I253-I255.

Churakov, S.V., and Wunder, B. (2004) Ab-initio calculations of the proton location in topaz-OH, $Al_2SiO_4(OH)_2$. Physics and Chemistry of Minerals, 31(3), 131-141.

D'Arco, P., Mustapha, S., Ferrabone, M., Noel, Y., De La Pierre, M., and Dovesi, R. (2013) Symmetry and random sampling of symmetry independent configurations for the simulation of disordered solids. Journal of Physics-Condensed Matter, 25(35).

Dovesi, R., Saunders, V.R., Roetti, C., Orlando, R., Zicovich-Wilson, C.M., Pascale, F., Civalleri, B., Doll, K., Harrison, N.M., Bush, I.J., D'Arco, P., and Llunell, M. (2009) CRYSTAL09 User's Manual. University of Torino, Torino.

Fletcher, R. (1970) A new approach to variable metric algorithms. The Computer Journal, 13(3), 317-322.

Gatta, G.D., Morgenroth, W., Dera, P., Petitgirard, S., and Liermann, H.P. (2014) Elastic behavior and pressure-induced structure evolution of topaz up to 45 GPa. Physics and Chemistry of Minerals, 41(8), 569-577.

Gatta, G.D., Nestola, F., and Ballaran, T.B. (2006a) Elastic behaviour and structural evolution of topaz at high pressure. Physics and Chemistry of Minerals, 33(4), 235-242.

Gatta, G.D., Nestola, F., Bromiley, G.D., and Loose, A. (2006b) New insight into crystal chemistry of topaz: A multi-methodological study. American Mineralogist, 91(11-12), 1839-1846.

Gatti, C., Saunders, V.R., and Roetti, C. (1994) Crystal-field effects on the topological properties of the electron-density in molecular-crystals - the case of urea. Journal of Chemical Physics, 101(12), 10686-10696.

Goldfarb, D. (1970) A family of variable-metric methods derived by variational means. Mathematics of Computation, 24, 23-26.

Haussuhl, S. (1993) Thermoelastic properties of beryl, topaz, diaspore, sanidine and periclase. Zeitschrift fuer Kristallographie, 204, 67-76.

Hill, R. (1952) The elastic behaviour of a crystalline aggregate. Proceedings of the Physical Society, London, Section A, 65, 349-354.

Kiefer, B., Stixrude, L., Hafner, J., and Kresse, G. (2001) Structure and elasticity of wadsleyite at high pressures. American Mineralogist, 86(11-12), 1387-1395.

Komatsu, K., Kagi, H., Marshall, W.G., Kuribayashi, T., Parise, J.B., and Kudoh, Y. (2008) Pressure dependence of the hydrogen-bond geometry in topaz-OD from neutron powder diffraction. American Mineralogist, 93(1), 217-227.

Komatsu, K., Kuribayashi, T., and Kudoh, Y. (2003) Effect of temperature and pressure on the crystal structure of topaz, $Al_2SiO_4(OH,F)_2$. Journal of Mineralogical and Petrological Sciences, 98, 167-180.

Lee, C.T., Yang, W.T., and Parr, R.G. (1988) Development of the Colle-Salvetti Correlation-Energy Formula into a Functional of the Electron-Density. Physical Review B, 37(2), 785-789.

Momma, K., and Izumi, F. (2011) VESTA 3 for three-dimensional visualization of crystal, volumetric and morphology data. Journal of Applied Crystallography, 44, 1272-1276.

Mustapha, S., D'Arco, P., De La Pierre, M., Noel, Y., Ferrabone, M., and Dovesi, R. (2013) On the use of symmetry in configurational analysis for the simulation of disordered solids. Journal of Physics-Condensed Matter, 25(10).

Nada, R., Catlow, C.R.A., Pisani, C., and Orlando, R. (1993) An ab-initio Hartree-Fock Perturbed-Cluster study of neutral defects in LiF. Modelling and Simulation in Materials Science and Engineering, 1(2), 165-187.

Nada, R., Nicholas, J.B., McCarthy, M.I., and Hess, A.C. (1996) Basis sets for ab initio periodic Hartree-Fock studies of zeolite/adsorbate interactions: He, Ne, and Ar in silica sodalite. International Journal of Quantum Chemistry, 60(4), 809-820.

Narejo, G., and Perger, W.F. (2010) First-principles computation of second-order elastic constants and equations of state for tetragonal $BaTiO_3$. Chemical Physics Letters, 493(4-6), 263-268.

-. (2011) First principle computations of second-order elastic constants (SOEC) and equations of state of rutile TiO_2. Physics Research International, 2011, 7 pages.

Northrup, P.A., Leinenweber, K., and Parise, J.B. (1994) The Location of H in the High-Pressure Synthetic $Al_2SiO_4(OH)_2$ Topaz Analog. American Mineralogist, 79(3-4), 401-404.

Nye, J.F. (1957) Physical properties of crystals. Oxford University Press, Oxford.

Ottonello, G., Civalleri, B., Ganguly, J., Perger, W.F., Belmonte, D., and Zuccolini, M.V. (2010) Thermo-chemical and thermo-physical properties of the high-pressure phase anhydrous B ($Mg_{14}Si_5O_{24}$): An ab-initio all-electron investigation. American Mineralogist, 95(4), 563-573.

Ottonello, G., Civalleri, B., Ganguly, J., Zuccolini, M.V., and Noel, Y. (2009) Thermophysical properties of the α–β–γ polymorphs of Mg_2SiO_4: a computational study. Physics and Chemistry of Minerals, 36(2), 87-106.

Pauling, L. (1928) The crystal structure of topaz. Proceedings of the National Academy of Sciences of the United States of America, 14, 603-606.

Perger, W.F. (2010) First-Principles Calculation of Second-Order Elastic Constants and Equations of State for Lithium Azide, LiN_3, and Lead Azide, $Pb(N_3)_2$. International Journal of Quantum Chemistry, 110(10), 1916-1922.

Perger, W.F., Criswell, J., Civalleri, B., and Dovesi, R. (2009) Ab-initio calculation of elastic constants of crystalline systems with the CRYSTAL code. Computer Physics Communications, 180(10), 1753-1759.

Pichavant, M., and Manning, D. (1984) Petrogenesis of tourmaline granites and topaz granites: the contribution of experimental data. Physics of the Earth and Planetary Interiors, 35, 31-50.

Prencipe, M., Pascale, F., Zicovich-Wilson, C.M., Saunders, V.R., Orlando, R., and Dovesi, R. (2004) The vibrational spectrum of calcite ($CaCO_3$): an ab initio quantum-mechanical calculation. Physics and Chemistry of Minerals, 31(8), 559-564.

Shanno, D.F. (1970) Conditioning of quasi-Newton methods for function minimization. Mathematics of Computation, 24, 647-656.

Taylor, R.P., and Fallick, A.E. (1997) The evolution of fluorine-rich felsic magmas: source dichotomy, magmatic convergence and the origins of topaz granite. Terra Nova, 9(3), 105-108.

Tsareva, G.M., Naumov, V.B., Kovalenko, V.I., Tsepin, A.I., and Babanskiy, A.D. (1992) Melt-inclusion data on the composition and crystallization conditions of the Spor Mountain topaz rhyolites. Geochemistry International, 29(5), 93-102.

Ugliengo, P., Viterbo, D., and Chiari, G. (1993) MOLDRAW: molecular graphic on a personal computer. Zeitschrift Fuer Kristallographie, 207, 9-23.

Ulian, G., Tosoni, S., and Valdre, G. (2013a) Comparison between Gaussian-type orbitals and plane wave ab initio density functional theory modeling of layer silicates: Talc [$Mg_3Si_4O_{10}(OH)_2$] as model system. Journal of Chemical Physics, 139(20).

Ulian, G., Tosoni, S., and Valdrè, G. (2014a) The compressional behaviour and the mechanical properties of talc [$Mg_3Si_4O_{10}(OH)_2$]: a density functional theory investigation. Physics and Chemistry of Minerals, 41(8), 639-650.

Ulian, G., and Valdrè, G. (2015a) Density functional investigation of the thermo-physical and thermo-chemical properties of 2M(1) muscovite. American Mineralogist, 100(4), 935-944.

-. (2015b) Density functional investigation of the thermophysical and thermochemical properties of talc $Mg_3Si_4O_{10}(OH)_2$. Physics and Chemistry of Minerals, 42(2), 151-162.

-. (2015c) Structural, vibrational and thermophysical properties of pyrophyllite by semi-empirical density functional modelling. Physics and Chemistry of Minerals, 42(7), 609-627.

Ulian, G., Valdrè, G., Corno, M., and Ugliengo, P. (2013b) Periodic ab initio bulk investigation of hydroxylapatite and type A carbonated apatite with both pseudopotential and all-electron basis sets for calcium atoms. American Mineralogist, 98(2-3), 410-416.

-. (2014b) DFT investigation of structural and vibrational properties of type B and mixed A-B carbonated hydroxylapatite. American Mineralogist, 99(1), 117-127.

Valenzano, L., Torres, F.J., Klaus, D., Pascale, F., Zicovich-Wilson, C.M., and Dovesi, R. (2006) Ab initio study of the vibrational spectrum and related properties of crystalline compounds; the case of $CaCO_3$ calcite. Zeitschrift Fur Physikalische Chemie-International Journal of Research in Physical Chemistry & Chemical Physics, 220(7), 893-912.

Wunder, B., Andrut, M., and Wirth, R. (1999) High-pressure synthesis and properties of OH-rich topaz. European Journal of Mineralogy, 11(5), 803-813.

Wunder, B., Rubie, D.C., Ross, C.R., Medenbach, O., Seifert, F., and Schreyer, W. (1993) Synthesis, stability, and properties of $Al_2SiO_4(OH)_2$: a fully hydrated analog of topaz. American Mineralogist, 78(3-4), 285-297.

Zhang, R.Y., Liou, J.G., and Shu, J.F. (2002) Hydroxyl-rich topaz in high-pressure and ultrahigh-pressure kyanite quartzites, with retrograde woodhouseite, from the Sulu terrane, eastern China. American Mineralogist, 87(4), 445-453.

LIST OF TABLES

Table 1. Experimental and theoretical refinement of different topaz structures

	T-F0H8	**T-F2H6**	**T-F4H4**	**T-F6H2**	**T-F7H1**	**T-F8H0**	**XRD[1]**	**Neutron Diffraction[2]**
Symmetry	*Pbn2$_1$*	*P1*	*Pbn2$_1$*	*P1*	*P1*	*Pbnm*	*Pbnm*	*Pbnm*
a (Å)	4.7808	4.7521	4.7215	4.7095	4.7051	4.7021	4.6601	4.7279
b (Å)	8.9792	8.9681	8.9643	8.9159	8.8932	8.8703	8.8260	8.9269
c (Å)	8.4900	8.4854	8.4721	8.4903	8.4971	8.5031	8.3778	8.4214
V_{cc} (Å^3)	364.5	361.6	358.6	356.5	355.5	354.7	344.6	355.4
Density (g/cm^3)	3.279	3.326	3.370	3.410	3.429	3.444	-	-

[1]Results by Gatta et al. (2006b) – $Al_2SiO_4(OH)_{0.25}F_{1.75}$; [2]Results by Komatsu et al. (2008) – $Al_2SiO_4(OH)(OD)$, where D is a deuterium atom.

Table 2. Results of the geometry optimization of T-F0H8 models with different hydrogen configurations.

Configuration	*ΔE (kJ/mol)*	*a (Å)*	*b (Å)*	*c* (Å)	*V* (Å^3)
H1 - H1	20.09	4.70681	9.02970	8.62742	366.67
H1 - H2	0.00	4.78079	8.97916	8.49003	364.46
H2 - H2*	50.92	4.76698	8.92043	8.63186	367.06

Notes: data with asterisk (*) are related to a probable saddle point, not a local minima.

Table 3. B3LYP atomic fractional coordinates in the symmetric topaz structures (T-F0H8, T-F4H4 and T-F8H0).

	DFT – present work				Experimental data			
Model	**Atom**	**x/a**	**y/b**	**z/c**	**Atom**	**x/a**	**y/b**	**z/c**
T-F0H8[a]	Al1	0.9006	0.1377	0.0790	Al	0.9050	0.1321	0.0798
	Al2	0.4053	0.3720	0.9194				
	H1	0.0361	0.2284	0.8279				
	H2	0.4311	0.1732	0.0808	H1	0.4430	0.1990	0.0880
	O1	0.7912	0.5278	0.2487	O1	0.7104	0.0262	0.2500
	O2	0.4516	0.7577	0.2464	O2	0.4439	0.7561	0.2500
	O3	0.7915	0.0108	0.9053				
	O4	0.2826	0.4979	0.0939	O3	0.2100	0.9929	0.0943
	O5	0.9240	0.7470	0.0645	OH	0.5906	0.2507	0.0659
	O6	0.4087	0.7520	0.9341				
	Si1	0.4022	0.9413	0.2500	Si	0.4019	0.9405	0.2500
T-F4H4	Al1	0.9034	0.1308	0.0794				
	Al2	0.4106	0.3685	0.9180				
	F1	0.4003	0.7478	0.9401				
	H1	0.4989	0.2517	0.1625				
	O1	0.7945	0.5326	0.2520				
	O2	0.4474	0.7564	0.2492				
	O3	0.7926	0.0116	0.9054				
	O4	0.2878	0.4905	0.0929				
	O5	0.9028	0.7533	0.0631				
	Si1	0.4012	0.9413	0.2503				
T-F8H0[a]	Al1	0.9013	0.1297	0.0838	Al	0.9030	0.1309	0.0828
	F1	0.8972	0.7526	0.0512	F	0.5982	0.2525	0.0561
	O1	0.6989	0.0334	0.2500	O1	0.7034	0.0321	0.2500
	O2	0.4625	0.7554	0.2500	O2	0.4577	0.7560	0.2500
	O3	0.2067	0.9877	0.0933	O3	0.2102	0.9892	0.0924
	Si1	0.3951	0.9392	0.2500	Si	0.3972	0.9404	0.2500

Experimental data for $Al_2SiO_4(OH)_2$ and $Al_2SiO_4F_2$ are taken from Northrup et al. (1994)

Table 4. Calculated elastic parameters, bulk (K_0) and axial moduli ($K_0(a)$, $K_0(b)$ and $K_0(c)$), their first derivatives (K') and corresponding zero-pressure (V_0, a_0, b_0 and c_0) values.

	T-F0H8	**T-F2H6**	**T-F4H4**	**T-F6H2**	**T-F7H1**	**T-F8H0**	**XRD**
K_0 (GPa)	145(3)	163(3)	165(3)	151(3)	164(3)	168(3)	158(6)
K'	4.2(5)	3.4(4)	3.4(4)	3.6(5)	3.0(4)	3.0(4)	3.3(4)
V_0 (Å^3)	365.4(9)	360.8(8)	357.6(8)	357.2(9)	355.0(8)	354.0(8)	-
K_0 *(a)* (GPa)	165(3)	174(3)	152(3)	134(3)	144(3)	144(3)	146(5)
K'(a)	3.6(4)	3.0(4)	3.8(5)	3.9(5)	3.3(4)	3.4(4)	4.6(3)
a_0 (Å)	4.785(5)	4.748(3)	4.717(4)	4.714(6)	4.703(4)	4.700(6)	-
K_0 *(b)* (GPa)	201(4)	234(4)	251(4)	222(4)	229(4)	227(4)	220(4)
K'(b)	3.7(5)	2.4(5)	2.0(4)	2.9(5)	2.5(5)	2.5(4)	2.6(3)
b_0 (Å)	8.985(5)	8.963(5)	8.958(5)	8.919(6)	8.888(5)	8.863(7)	-
K_0 *(c)* (GPa)	100(3)	113(3)	125(4)	125(3)	141(3)	150(3)	132(4)
K'(c)	4.8(5)	4.1(5)	3.9(4)	3.7(4)	3.0(3)	2.9(4)	3.3(3)
c_0 (Å)	8.503(10)	8.481(9)	8.466(9)	8.499(10)	8.493(7)	8.498(10)	-

Notes: XRD values are from the experimental work of Gatta et al. (2014) – $Al_2SiO_4(OH)_{0.25}F_{1.75}$

Table 5. Bond lengths (Å), polyhedral volumes (Å^3) and bond angles (°) in the different topaz models at selected pressures.

	P1	P2	P3	P4	P5
T-F0H8					
Pressure (GPa)	0.7	7.0	18.9	34.3	52.7
< Al – O >	1.9167	1.8949	1.8660	1.8372	1.8077
< Al–(O,F)–Al>	138.9	136.7	133.9	131.6	129.6
< V (Al-octah) >	9.3068	9.0083	8.6160	8.2302	7.8436
< Si – O >	1.6660	1.6533	1.6359	1.6180	1.5998
< V (Si-tetrah) >	2.3672	2.3142	2.2429	2.1709	2.0995
< H – O >	0.9658	0.9668	0.9679	0.9695	0.9713
< H–O–Al>	105.7	105.8	105.9	105.9	105.9
T-F2H6					
Pressure (GPa)	1.1	6.9	19.0	34.0	51.5
< Al – O >	1.9027	1.8842	1.8563	1.8283	1.7997
< Al–(O,F)–Al>	143.5	140.6	136.5	133.0	130.4
< V (Al-octah) >	9.1086	8.8554	8.4831	8.1146	7.7435
< Si – O >	1.6613	1.6508	1.6334	1.6158	1.5978
< V (Si-tetrah) >	2.3476	2.3040	2.2324	2.1613	2.0897
< H – O >	0.9620	0.9642	0.9646	0.9651	0.9653
< H–O–Al>	108.7	108.0	108.3	108.7	108.9
T-F4H4					
Pressure (GPa)	1.1	9.2	22.1	37.8	52.2
< Al – (F,O) >	1.8964	1.8740	1.8464	1.8187	1.7907
< Al–(O,F)–Al >	142.5	139.7	136.3	133.4	131.1
< V (Al-octah) >	9.0066	8.7082	8.3466	7.9879	7.6313
< Si – O >	1.6622	1.6479	1.6303	1.6120	1.5940
< V (Si-tetrah) >	2.3527	2.2931	2.2205	2.1464	2.0754
< H – O >	0.9615	0.9615	0.9608	0.9583	0.9555
< H–O–Al>	109.6	110.8	112.3	113.6	114.6
T-F6H2					
Pressure (GPa)	1.1	6.9	19.0	34.0	51.5
< Al – O >	1.8867	1.8597	1.8368	1.8058	1.7848
< Al–(O,F)–Al>	147.1	143.1	139.6	135.0	132.2
< V (Al-octah) >	8.8565	8.5047	8.2122	7.8195	7.5558
< Si – O >	1.6609	1.6431	1.6278	1.6069	1.5930
< V (Si-tetrah) >	2.3479	2.2737	2.2104	2.1258	2.0700
< H – O >	0.9616	0.9611	0.9605	0.9589	0.9571
< H–O–Al>	109.3	110.7	112.0	113.6	114.4
T-F7H1					
Pressure (GPa)	1.1	6.9	19.0	34.0	51.5
< Al – O >	1.8799	1.8632	1.8364	1.8056	1.7849
< Al–(O,F)–Al>	147.7	145.1	140.8	135.9	133.1
< V (Al-octah) >	8.7630	8.5460	8.2043	7.8161	7.5571
< Si – O >	1.6557	1.6446	1.6269	1.6062	1.5927
< V (Si-tetrah) >	2.3270	2.2809	2.2083	2.1241	2.0698
< H – O >	0.9609	0.9607	0.9602	0.9582	0.9562
< H–O–Al>	110.8	111.7	113.1	114.7	115.4

T-F8H0

Pressure (GPa)	1.2	9.4	22.1	37.1	50.6
<Al – (F,O)>	1.8758	1.8533	1.8270	1.7995	1.7764
< Al–(O,F)–Al >	148.6	145.3	141.1	137.9	133.7
< V (Al-octah) >	8.6941	8.4057	8.0755	7.7319	7.4505
<Si – O>	1.6587	1.6434	1.6250	1.6042	1.5896
< V (Si-tetrah) >	2.3402	2.2769	2.2015	2.1187	2.0594

Table 6. Calculated elastic constants (GPa), bulk (K), shear (μ) and Young's (E) moduli in GPa and mean shear and longitudinal wave velocities (v_s and v_l, respectively) in km/s at 0 GPa for the different topaz models.

SOEC Component	**T-F0H8**	**T-F2H6**	**T-F4H4**	**T-F6H2**	**T-F7H1**	**T-F8H0**	**Exp.**
C_{11}	302.30	285.07	259.50	267.36	269.04	270.31	278.5(5)
C_{12}	104.74	111.97	119.40	118.25	117.91	119.41	120.4(2)
C_{13}	78.32	75.543	79.27	78.14	79.71	81.01	80.6(1)
C_{22}	340.94	343.05	342.94	337.48	334.14	331.07	344.8(6)
C_{23}	77.04	79.19	79.86	80.55	80.49	81.21	80.3(1)
C_{33}	229.79	245.49	256.02	278.44	288.70	295.98	292.5(5)
C_{44}	102.69	103.76	104.59	104.16	103.78	103.47	108.6(8)
C_{55}	111.34	115.61	122.23	125.16	126.63	127.88	132.9(8)
C_{66}	123.90	126.16	127.47	127.04	126.86	126.32	130.3(8)
K_V	154.80	156.33	157.28	159.68	160.90	162.29	-
K_R	149.12	151.50	153.03	156.96	158.89	160.68	-
K_{VRH}	151.96	153.92	155.15	158.32	159.89	161.49	-
μ_V	108.45	109.56	109.52	111.69	112.37	112.58	-
μ_R	106.61	107.46	106.55	109.27	109.95	110.13	-
μ_{VRH}	107.53	108.51	108.03	110.48	111.16	111.36	-
E_{VRH}	261.02	263.59	263.05	268.90	270.74	271.64	-
v_s	5.73	5.71	5.66	5.69	5.69	5.69	-
v_p	9.73	9.71	9.67	9.71	9.73	9.74	-

Eperimental data taken from the work of Haussuhl (1993) – $Al_2SiO_4F_2$.

FIGURE CAPTIONS

Figure 1. Polyhedral models of (a) T-F0H8, (b) T-F2H6, (c) T-F4H4, (d) T-F6H2, (e) T-F7H1 and (f) T-F8H0 structures as seen from the [100] direction. In the symmetric structures (a, c and f) the irreducible atoms are labelled.

Figure 2. (a) Topaz unit cell volume as a function of fluorine content. (b) Relative axial variations related to the fluorine content. (c) Topaz density as a function of fluorine content.

Figure 3. (a) ΔE (Ha) *vs* Volume ($Å^3$) plot for the different topaz models. (b) Plot of topaz relative compression as a function of pressure, for the different F contents, together with previous experimental results (Gatta et al., 2014; Gatta et al., 2006a; Komatsu et al., 2003). (c,d) Zoom of the black-boxed and red-boxed highlighted section of (b), respectively.

Figure 4. Relative axial compression (l/l_0) of the different topaz models, as a function of pressure.

Figure 1a

(a)

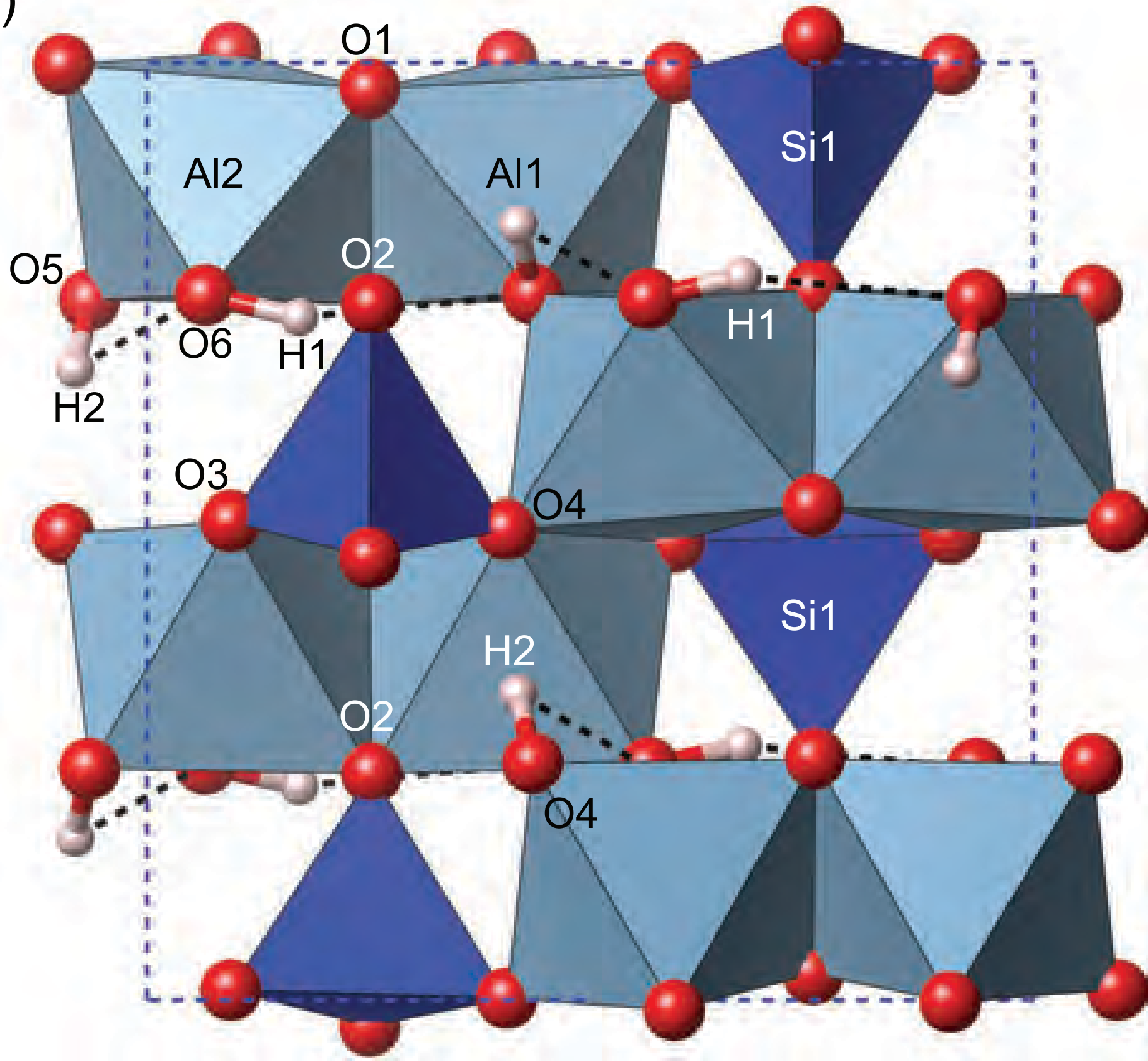

Figure 1b
(b)

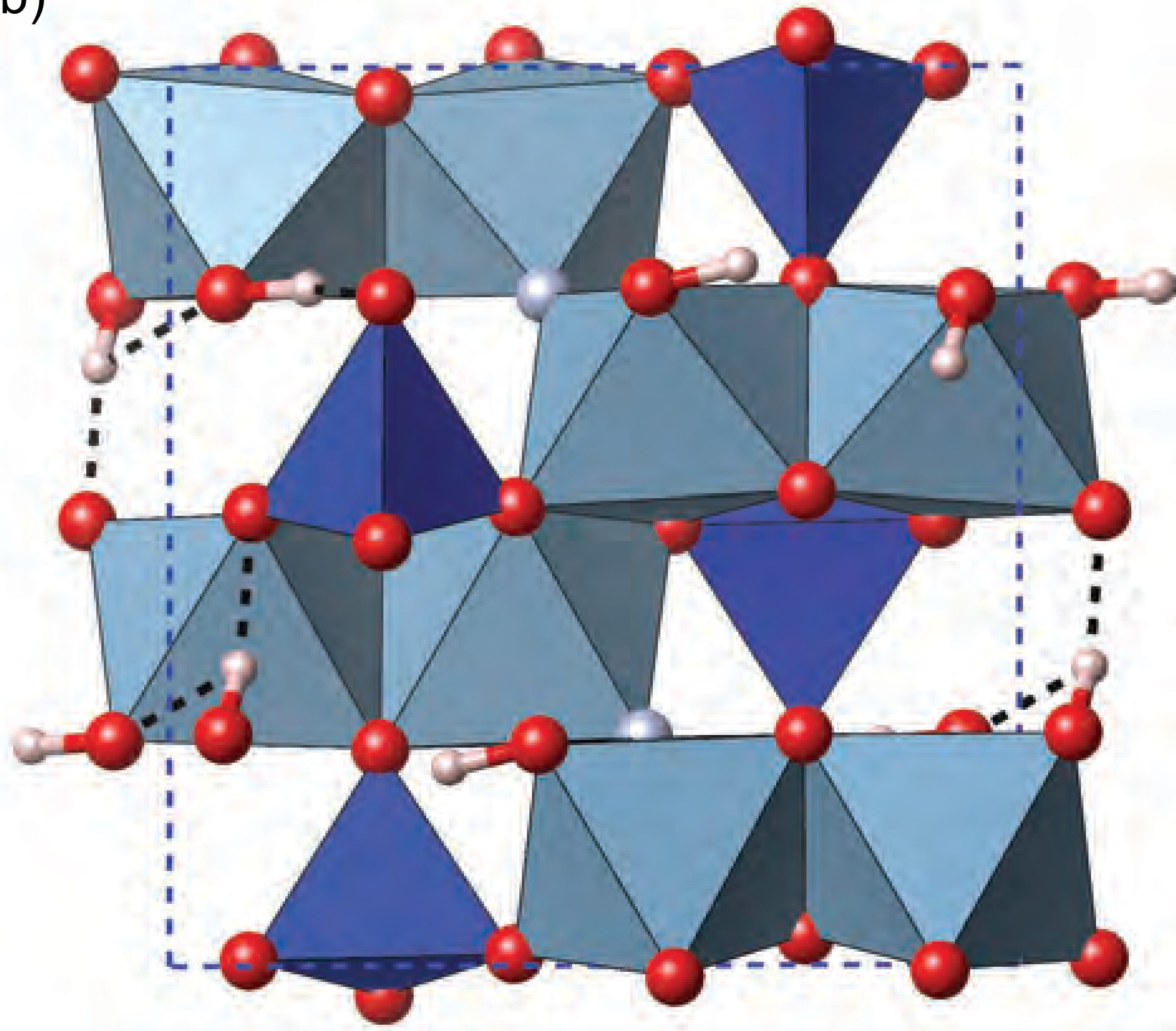

Figure 1c
(c)

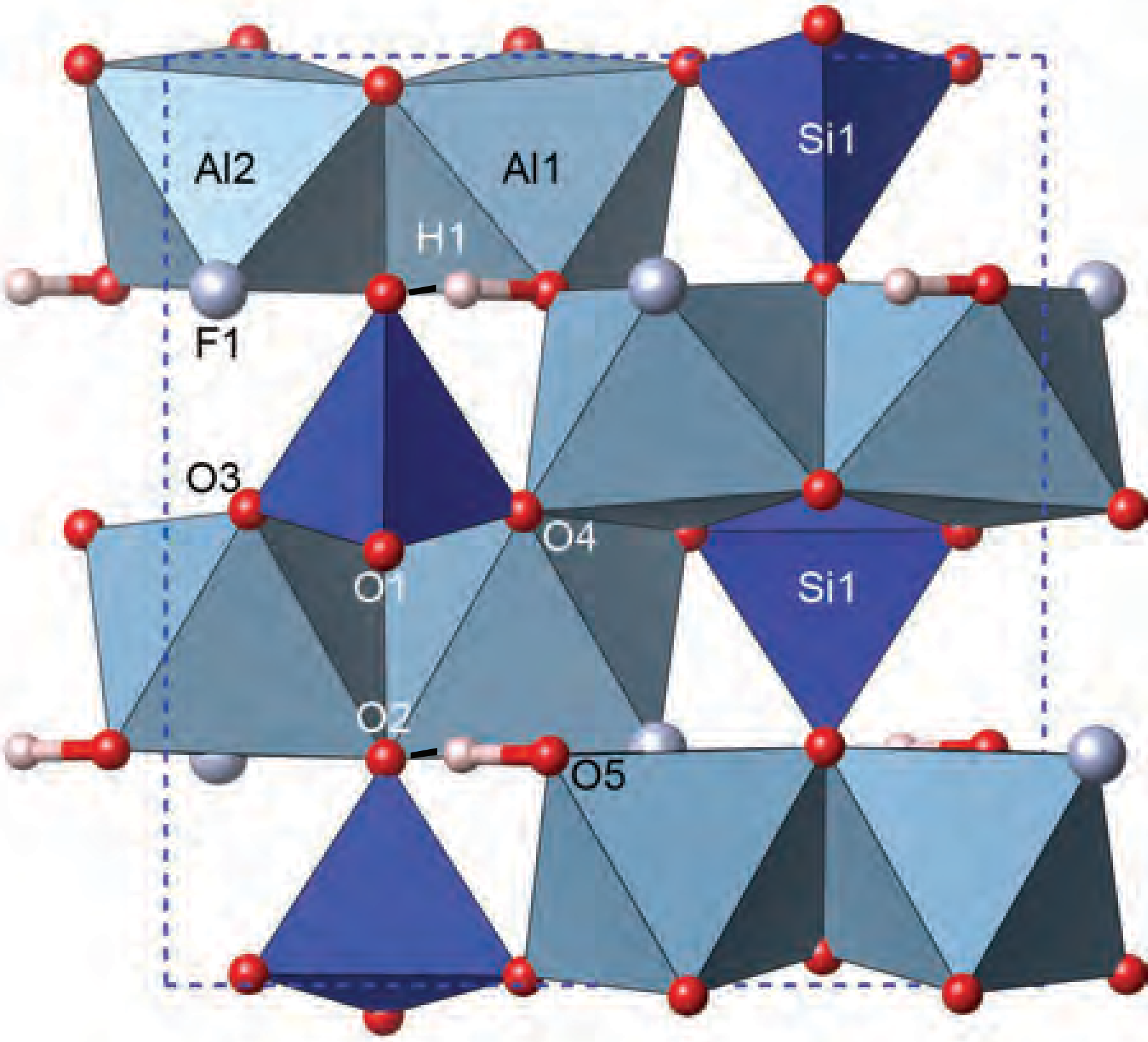

Figure 1d
(d)

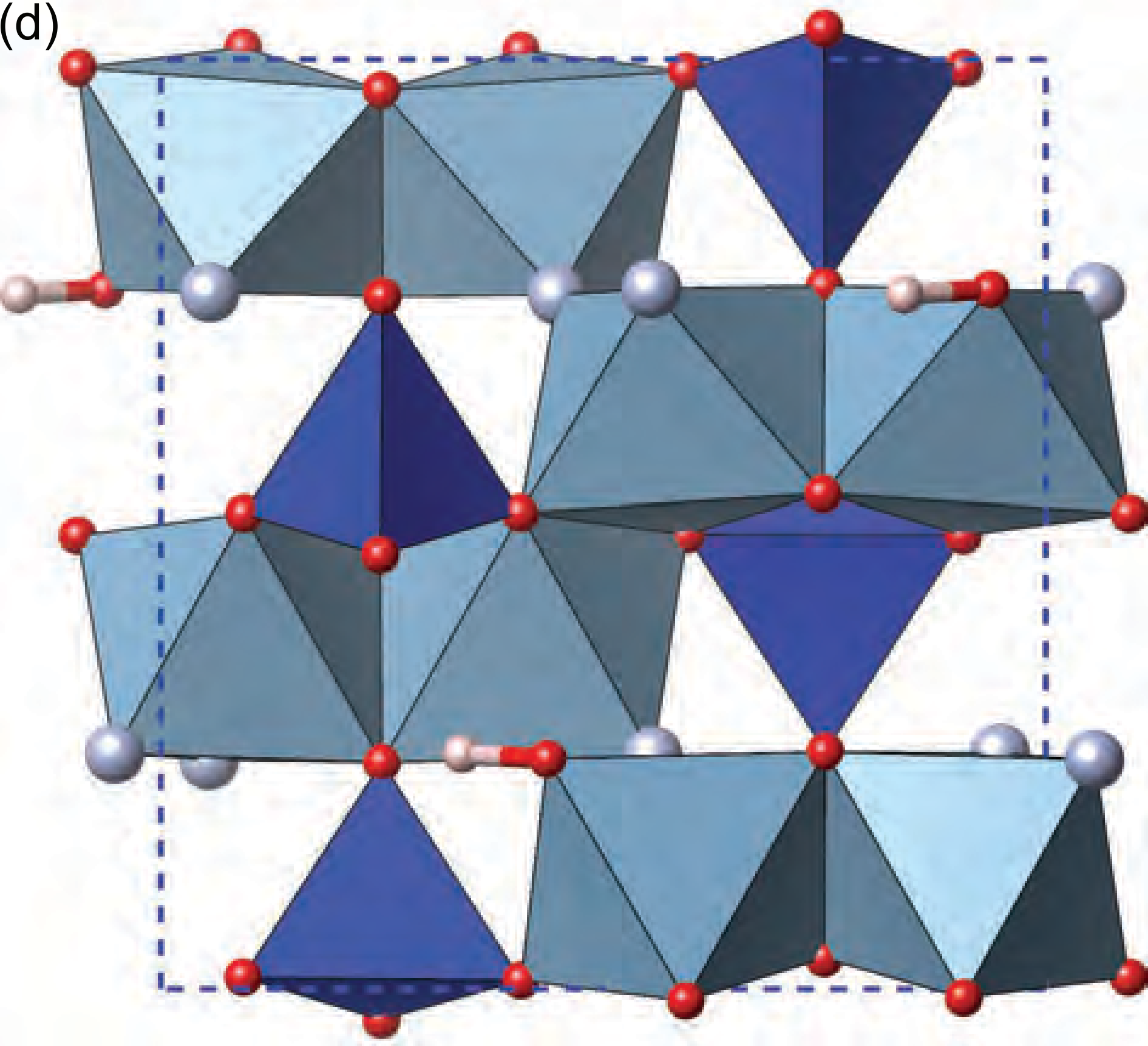

Figure 1e
(e)

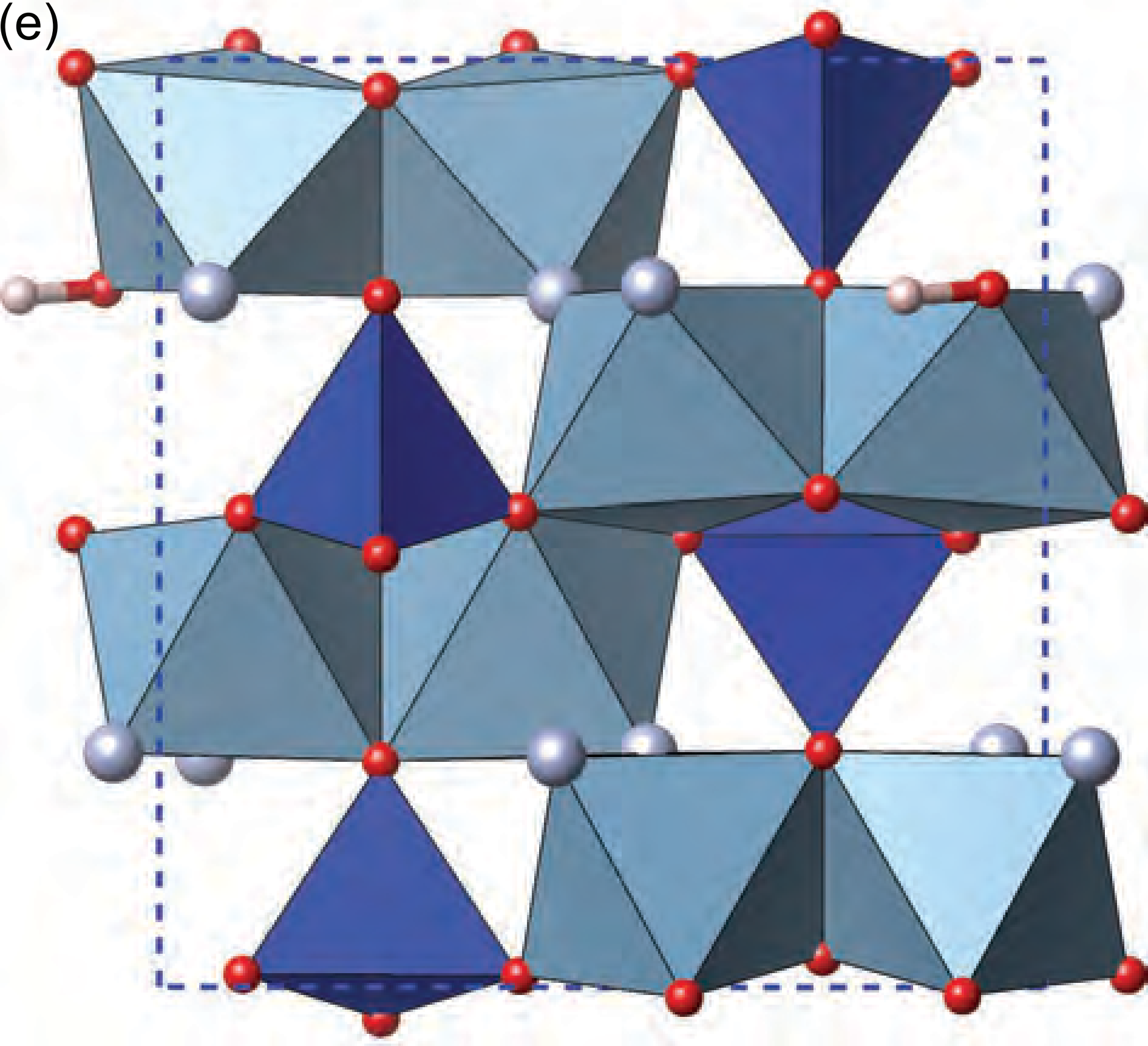

Figure 1f

(f)

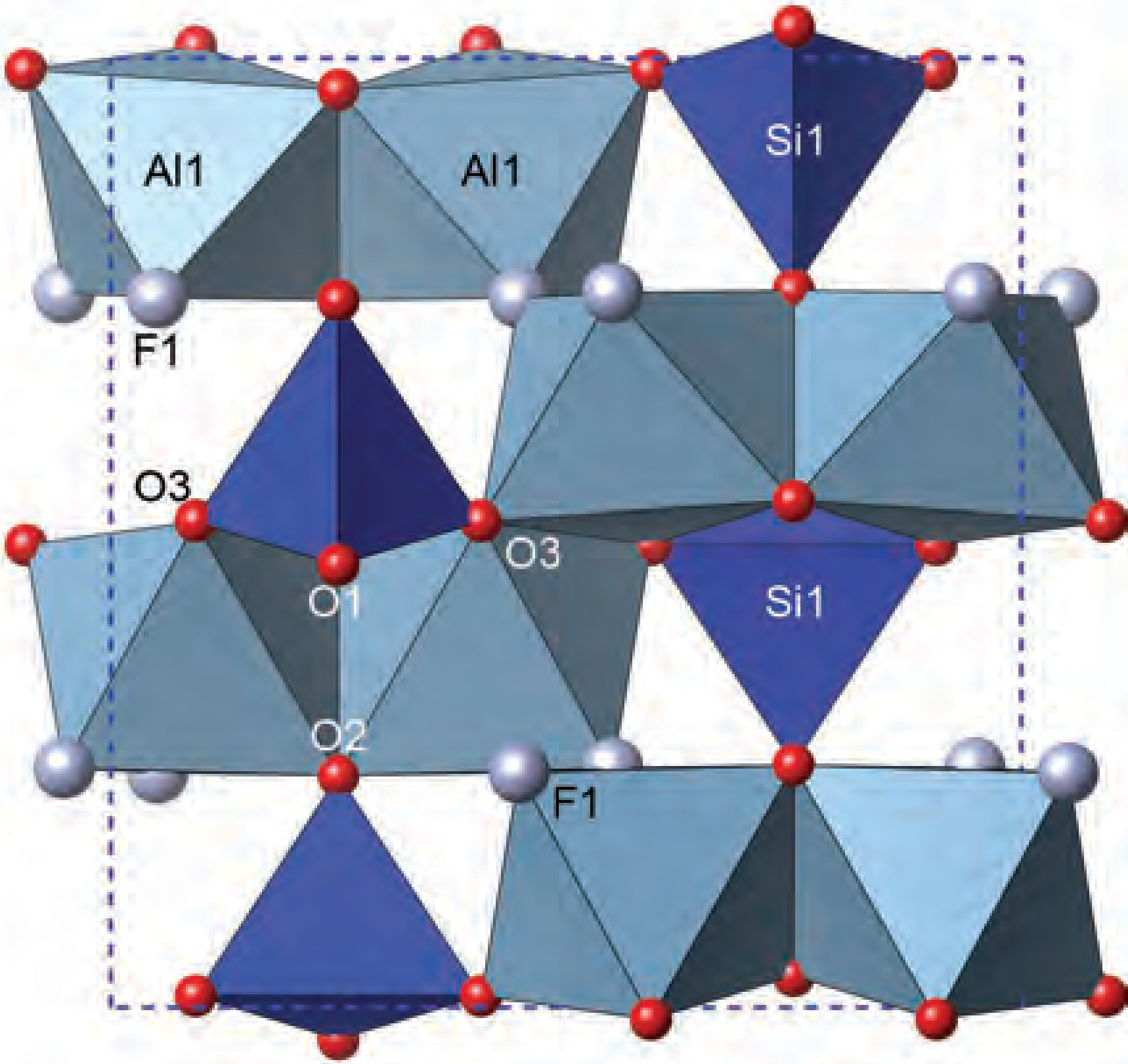

Figure 2a

(a)

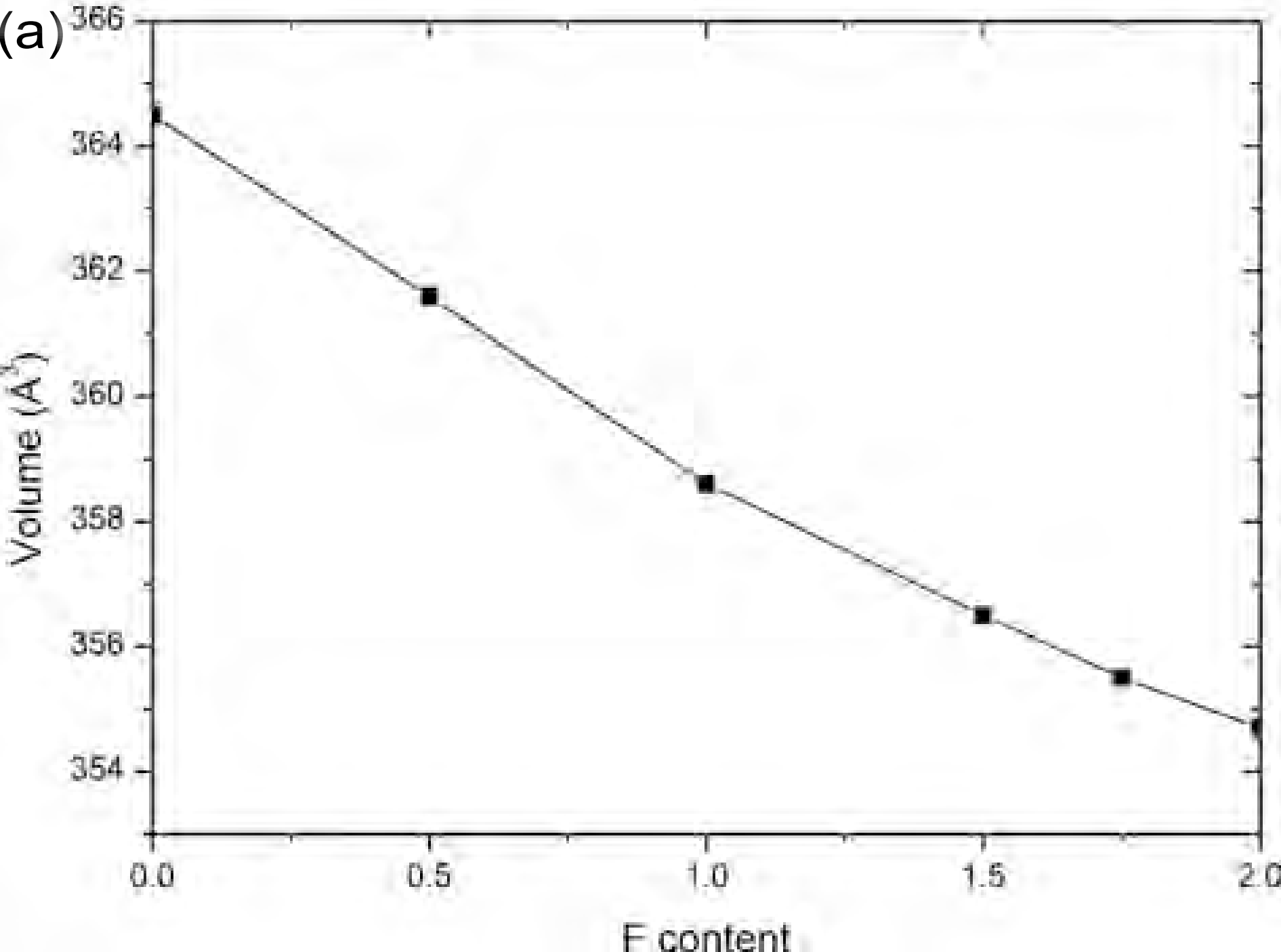

Figure 2b

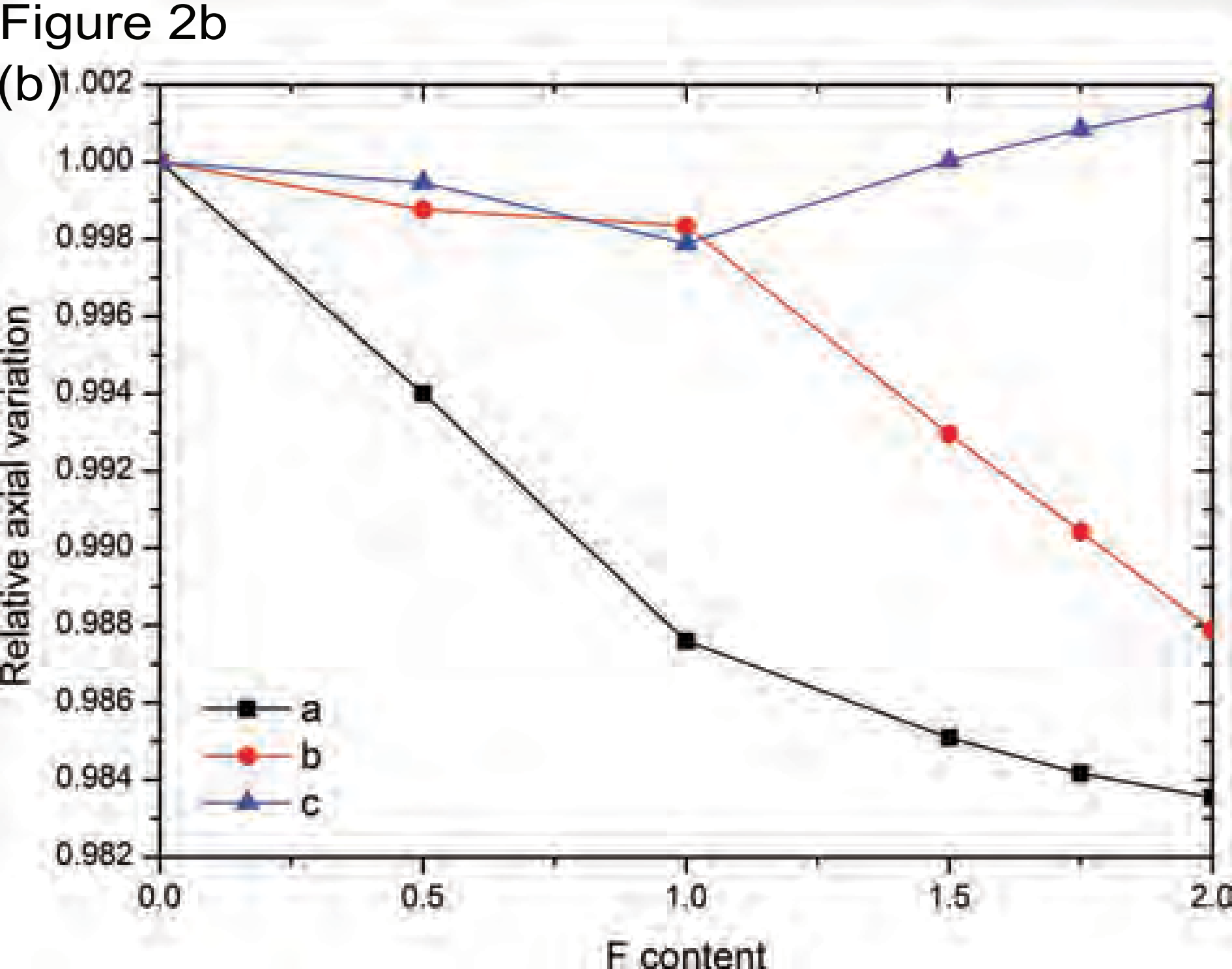
(b)
1.002
1.000
0.998
0.996
0.994
0.992
0.990
0.988
0.986
0.984
0.982
Relative axial variation
a
b
c
0.0
0.5
1.0
1.5
2.0
F content

Figure 2c

(c)

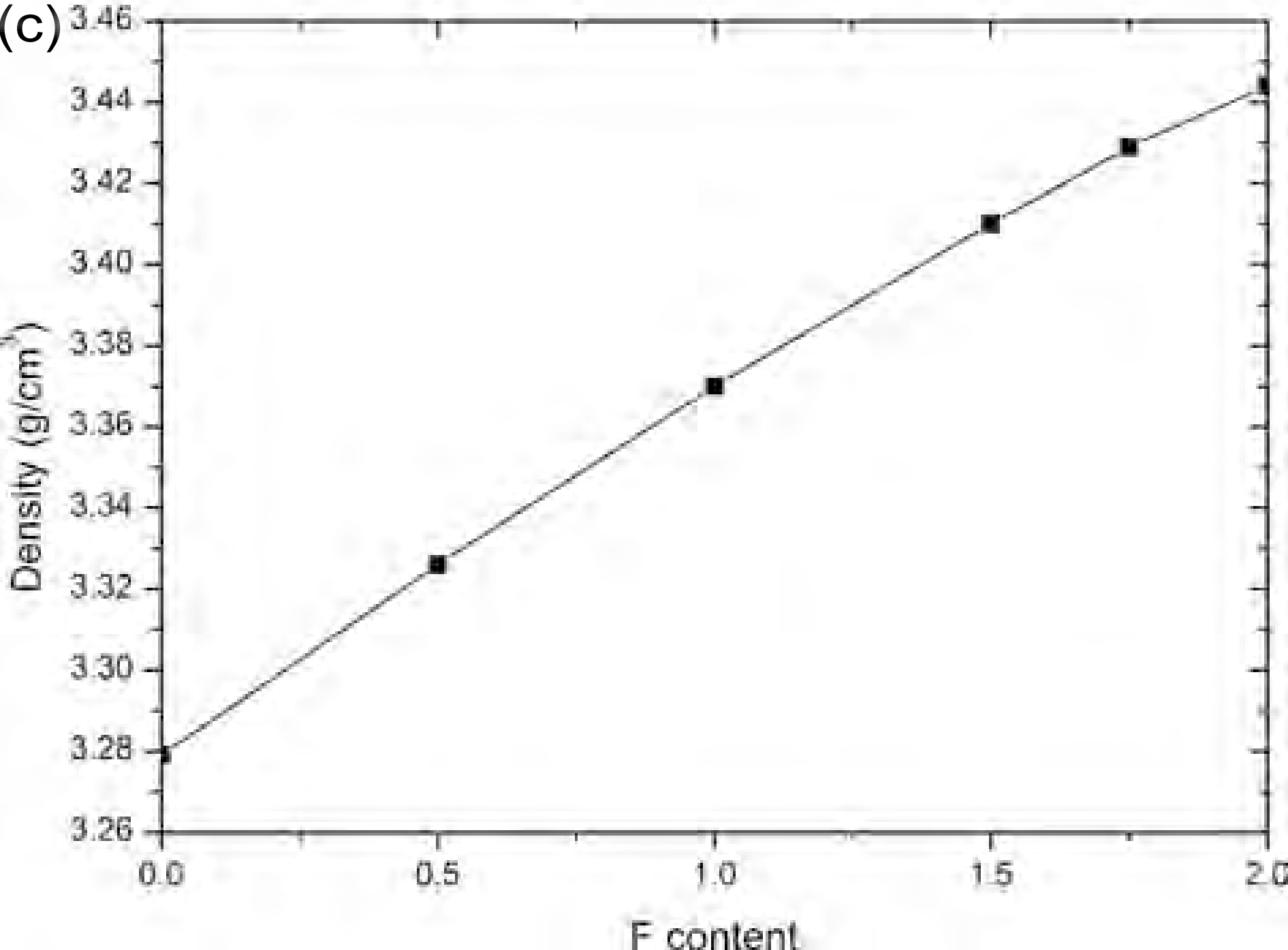
3.46
3.44
3.42
3.40
3.38
3.36
3.34
3.32
3.30
3.28
3.26
Density (g/cm^3)
0.0
0.5
1.0
1.5
2.0
F content

Figure 3a
(a)

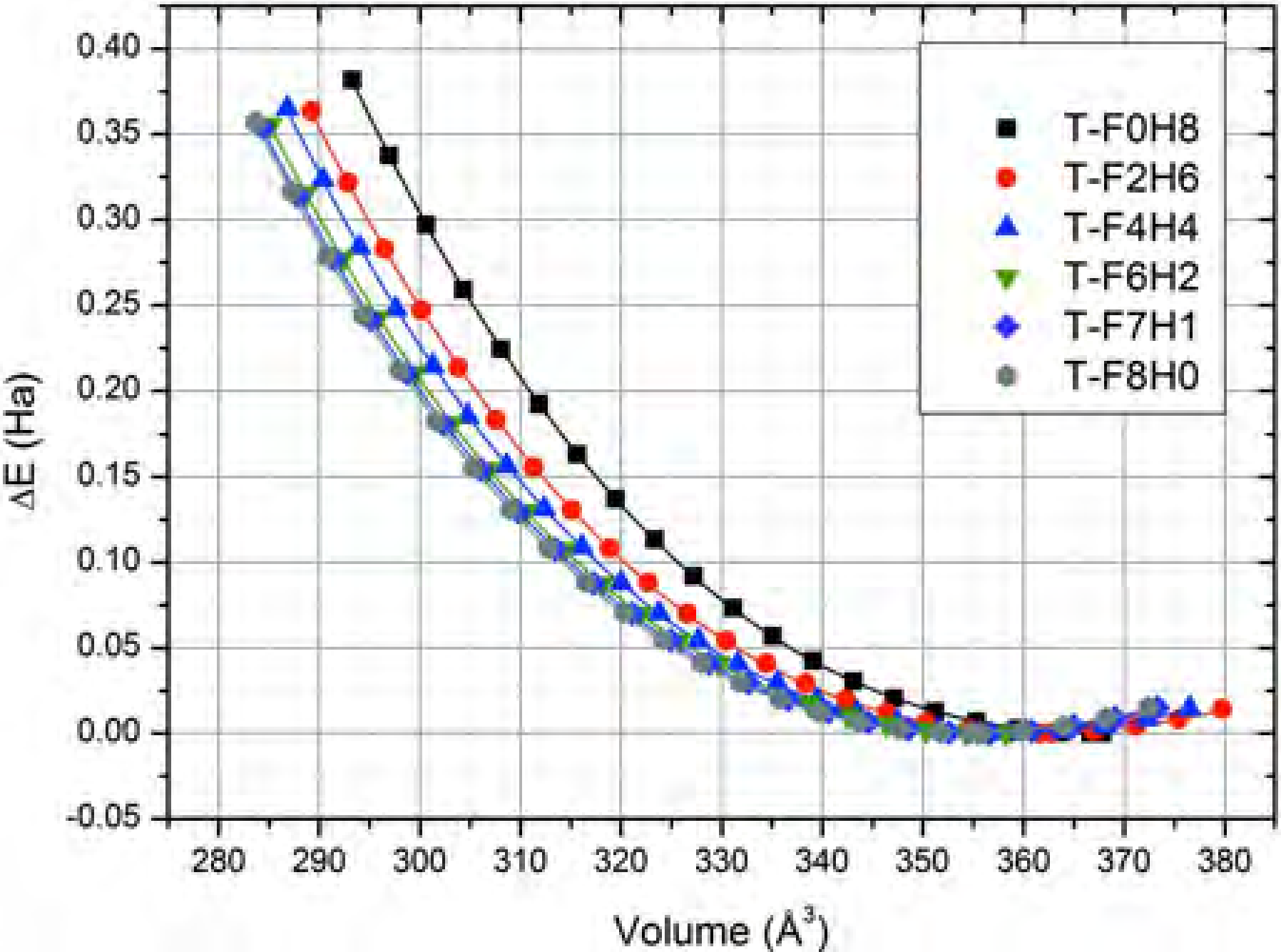
0.40
0.35
0.30
0.25
0.20
0.15
0.10
0.05
0.00
-0.05
ΔE (Ha)
280
290
300
310
320
330
340
350
360
370
380
Volume (Å^3)
T-F0H8
T-F2H6
T-F4H4
T-F6H2
T-F7H1
T-F8H0

Figure 3b
(b)

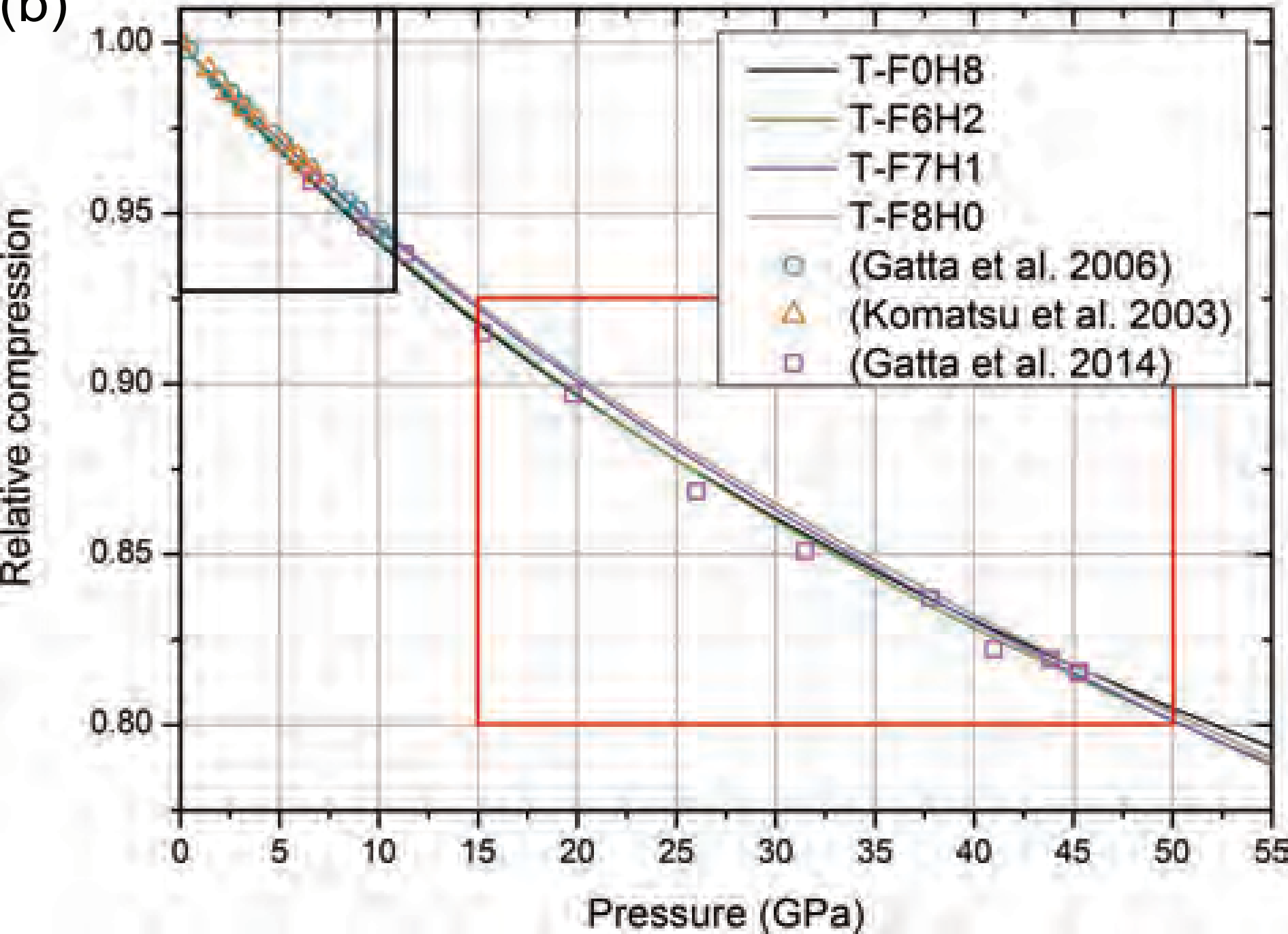
T-F0H8
T-F6H2
T-F7H1
T-F8H0
(Gatta et al. 2006)
(Komatsu et al. 2003)
(Gatta et al. 2014)
Relative compression
1.00
0.95
0.90
0.85
0.80
0
5
10
15
20
25
30
35
40
45
50
55
Pressure (GPa)

Figure 3c

(c)

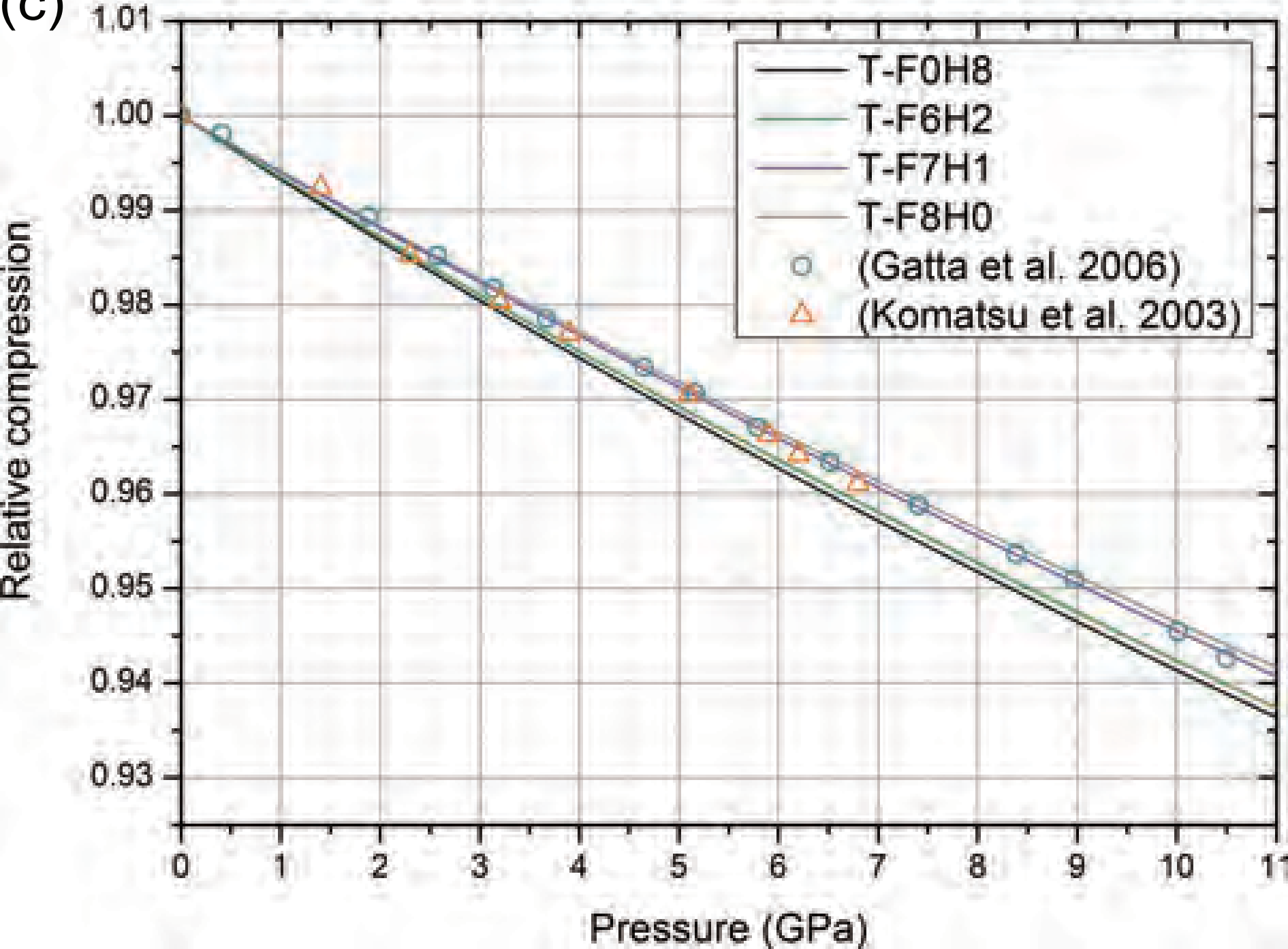
T-F0H8
T-F6H2
T-F7H1
T-F8H0
(Gatta et al. 2006)
(Komatsu et al. 2003)
Relative compression
Pressure (GPa)
1.01
1.00
0.99
0.98
0.97
0.96
0.95
0.94
0.93
0
1
2
3
4
5
6
7
8
9
10
11

Figure 3d
(d)

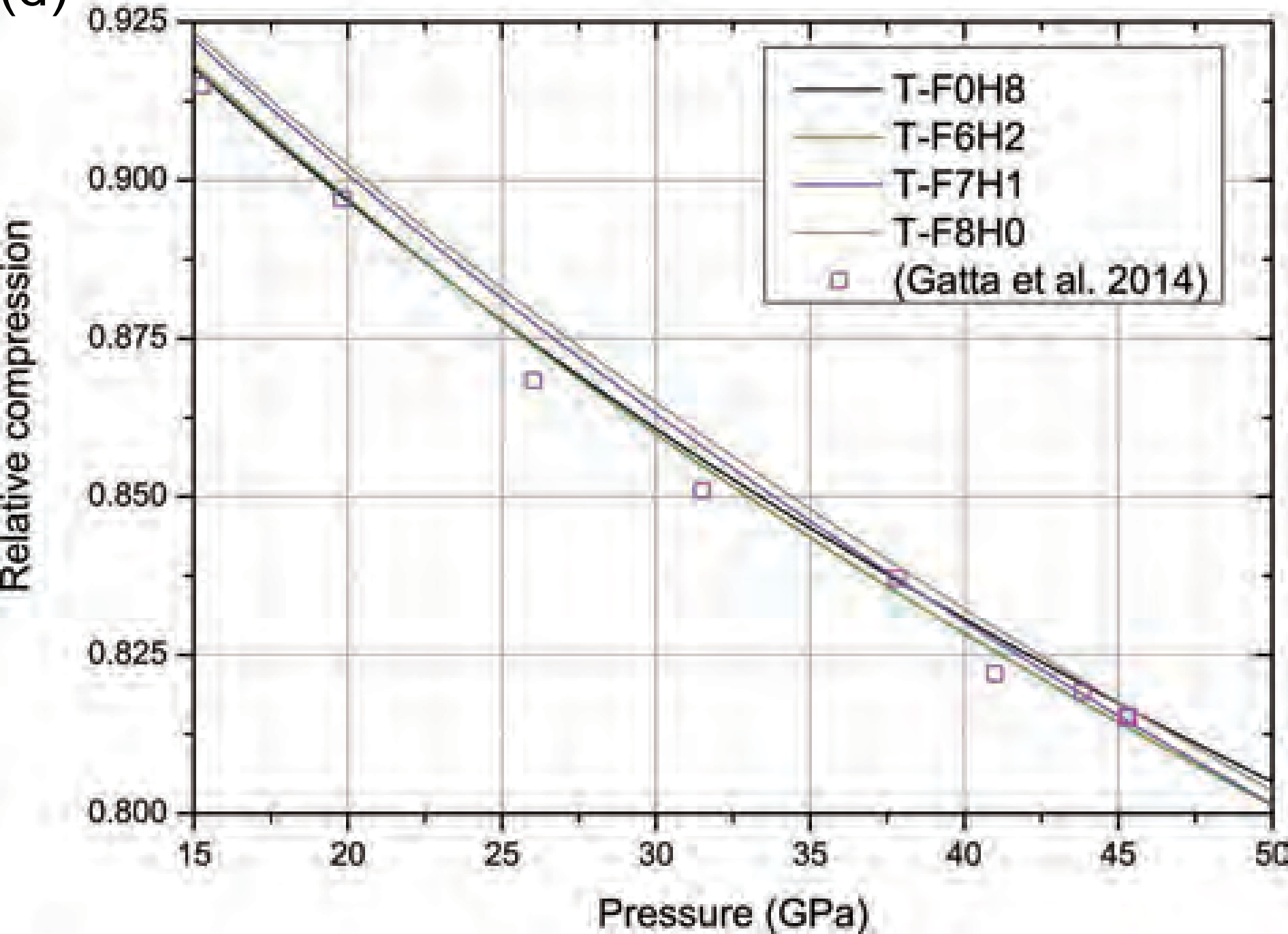
0.925
0.900
0.875
0.850
0.825
0.800
Relative compression
15
20
25
30
35
40
45
50
Pressure (GPa)
T-F0H8
T-F6H2
T-F7H1
T-F8H0
(Gatta et al. 2014)

Figure 4

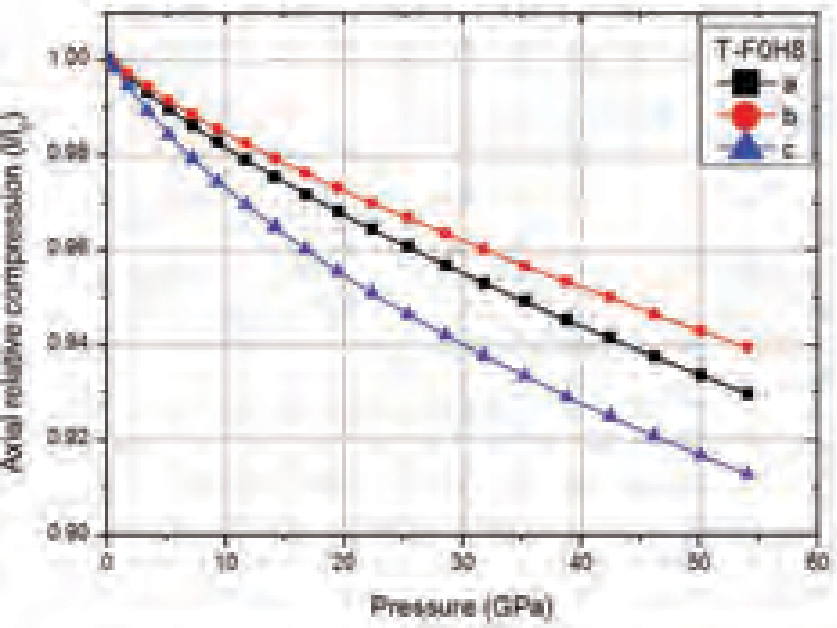
T-F0H8
a
b
c
Axial relative compression (l/l0)
Pressure (GPa)

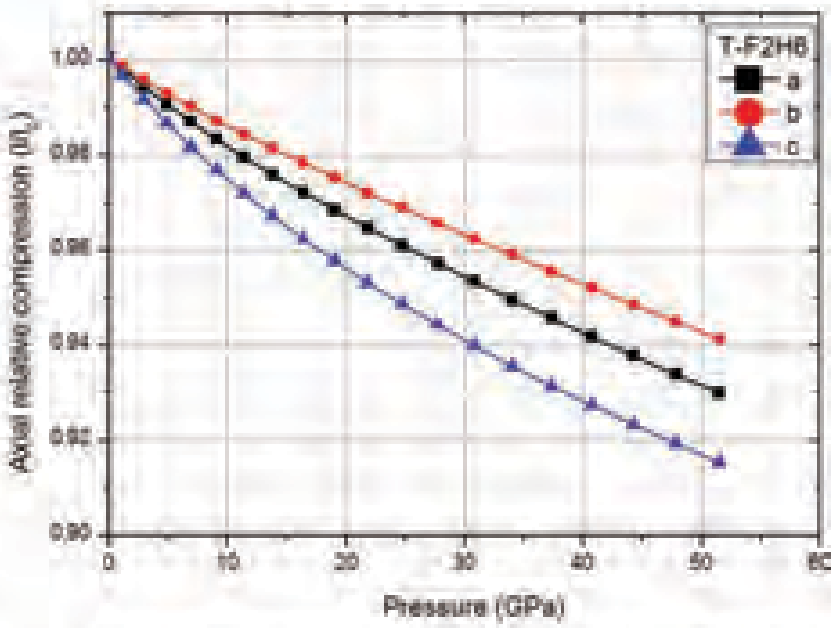
T-F2H6
a
b
c
Axial relative compression (l/l0)
Pressure (GPa)

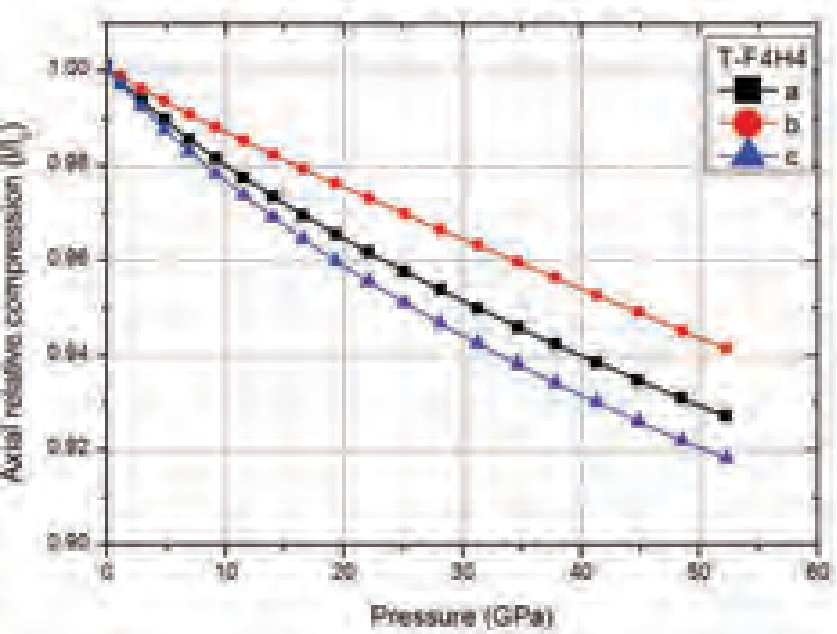
T-F4H4
a
b
c
Axial relative compression (l/l0)
Pressure (GPa)

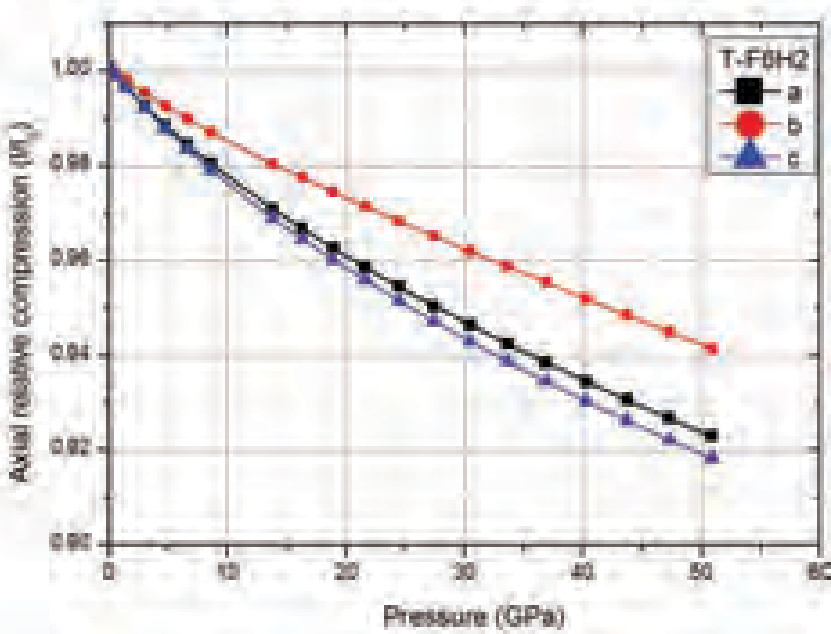
T-F6H2
a
b
c
Axial relative compression (l/l0)
Pressure (GPa)

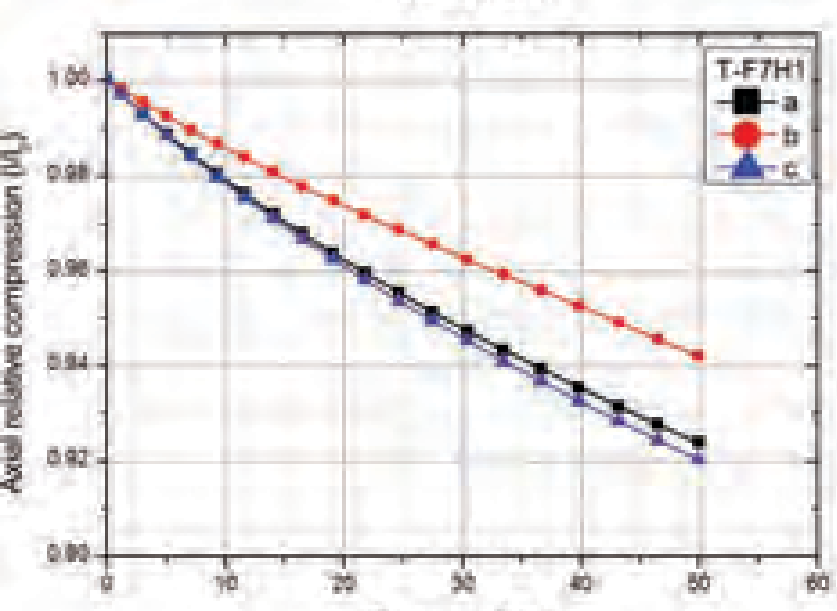
T-F7H1
a
b
c
Axial relative compression (l/l0)
Pressure (GPa)

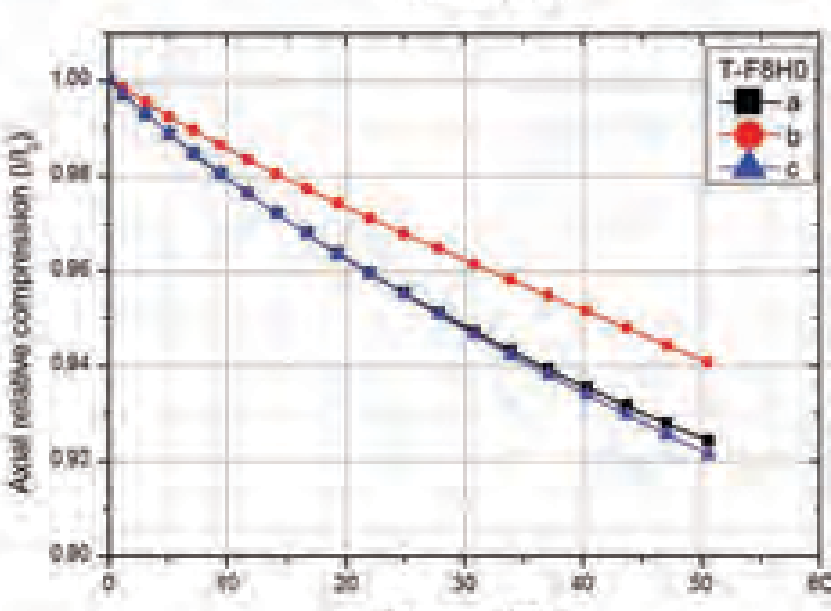
T-F8H0
a
b
c
Axial relative compression (l/l0)
Pressure (GPa)